

1 **Generation of turbulence in Kelvin-Helmholtz vortices at the Earth's magnetopause:**
2 **Magnetospheric Multiscale observations**

3 **H. Hasegawa¹, T. K. M. Nakamura², D. J. Gershman³, Y. Nariyuki⁴, A. F.-Viñas³, B. L.**
4 **Giles³, B. Lavraud⁵, C. T. Russell⁶, Y. V. Khotyaintsev⁷, R. E. Ergun⁸, and Y. Saito¹**

5 ¹Institute of Space and Astronautical Science, Japan Aerospace Exploration Agency,
6 Sagamihara, Japan

7 ²Space Research Institute, Austrian Academy of Sciences, Graz, Austria

8 ³NASA Goddard Space Flight Center, Greenbelt, MD, USA

9 ⁴Faculty of Human Development, University of Toyama, Toyama, Japan

10 ⁵Institut de Recherche en Astrophysique et Planétologie, CNRS, UPS, CNES, Université de
11 Toulouse, Toulouse, France

12 ⁶Department of Earth, Planetary, and Space Sciences, University of California, Los Angeles,
13 California, USA

14 ⁷Swedish Institute of Space Physics, Uppsala, Sweden

15 ⁸Department of Astrophysical and Planetary Sciences, University of Colorado, Boulder,
16 Colorado, USA

17
18 Corresponding author: Hiroshi Hasegawa (hase@stp.isas.jaxa.jp)

19
20 **Key Points:**

- 21 • The Kelvin-Helmholtz instability amplifies electromagnetic fluctuations in the
22 magnetopause boundary layer
- 23 • The turbulent fluctuations in the vortices may not be due to propagating waves but to
24 magnetic structures, i.e., interlaced flux tubes
- 25 • The turbulence at sub-ion scales in an early nonlinear phase of the instability is likely a
26 consequence of vortex induced reconnection
27

28 **Abstract**

29 The Kelvin-Helmholtz instability (KHI) at Earth's magnetopause and associated turbulence are
30 suggested to play a role in the transport of mass and momentum from the solar wind into Earth's
31 magnetosphere. We investigate electromagnetic turbulence observed in KH vortices encountered
32 at the dusk flank magnetopause by the Magnetospheric Multiscale (MMS) spacecraft under
33 northward interplanetary magnetic field (IMF) conditions in order to reveal its generation
34 process, mode properties, and role. A comparison with another MMS event at the dayside
35 magnetopause with reconnection but no KHI signatures under a similar IMF condition indicates
36 that while high-latitude magnetopause reconnection excites a modest level of turbulence in the
37 dayside low-latitude boundary layer, the KHI further amplifies the turbulence, leading to
38 magnetic energy spectra with a power-law index $-5/3$ at magnetohydrodynamic scales even in its
39 early nonlinear phase. The mode of the electromagnetic turbulence is analyzed with a single-
40 spacecraft method based on Ampère's law, developed by Bellan (2016), for estimating wave
41 vectors as a function of spacecraft-frame frequency. The results suggest that the turbulence does
42 not consist of propagating normal-mode waves, but is due to interlaced magnetic flux tubes
43 advected by plasma flows in the vortices. The turbulence at sub-ion scales in the early nonlinear
44 phase of the KHI may not be the cause of the plasma transport across the magnetopause, but
45 rather a consequence of three-dimensional vortex induced reconnection, the process that can
46 cause an efficient transport by producing tangled reconnected field lines.

47 **Plain Language Summary**

48 Turbulence is ubiquitous in nature and plays an important role in material mixing and energy
49 transport. Turbulence in space plasmas is characterized by fluctuations of flow velocity and/or
50 electromagnetic fields over a broad frequency range and/or length scales, and is believed to be
51 the key to efficient plasma transport and heating. However, its generation mechanism is not fully
52 understood because turbulence in space is often fully developed or already relaxed when
53 observed. By analyzing high-resolution plasma and electromagnetic field data taken by the
54 Magnetospheric Multiscale spacecraft, we study the generation process of electromagnetic
55 turbulence at the outer boundary of Earth's magnetosphere, called the magnetopause, where
56 either a flow shear-driven Kelvin-Helmholtz instability or magnetic reconnection or both could
57 drive turbulence. It is shown that while dayside reconnection generates a modest level of
58 turbulence at the magnetopause near noon, the flow shear instability further amplifies the
59 turbulence at the flank magnetopause. Our analysis also suggests that the turbulence may not be
60 the primary cause of plasma transport from solar wind into the magnetosphere, but rather a
61 consequence of the flow shear-induced reconnection that is likely the primary cause of plasma
62 transport at the dayside flank under northward solar wind magnetic field conditions.

63 **1 Introduction**

64 Turbulence is ubiquitous in nature, such as in ocean (Smyth & Moum, 2012), planetary
65 atmospheres (Wyngaard, 1992; Vasavada & Showman, 2005), solar/stellar convection zones
66 (Miesch et al., 2000), accretion disks (Balbus & Hawley, 1998), and interstellar gas (Gaensler et
67 al., 2011), and is believed to play a key role in material mixing and energy transfer in both
68 configuration and wave number space. Turbulence in plasmas is characterized by broadband
69 fluctuations of not only flows but also electromagnetic fields, and has been extensively and
70 intensively studied in the solar wind community (e.g., Bruno & Carbone, 2013; Chen, 2016).
71 While the turbulent cascade and dissipation processes at kinetic scales have been the focus of

72 recent studies on space plasma turbulence (Alexandrova et al., 2009, 2013; Narita, Nakamura, et
73 al., 2016; Sahraoui et al., 2009; Phan et al., 2018), its generation mechanism is not fully
74 understood; the turbulent energy injection process remains an open issue. This is partly because
75 turbulence observed in the solar wind near 1 AU is often fully developed or may already be
76 relaxed, leaving no or little information on how it is generated, although Parker Solar Probe (Fox
77 et al., 2016), launched in 2018 and making in-situ measurements of the inner heliosphere and
78 solar corona, is going to reveal the generation, or at least evolution, process of solar wind
79 turbulence.

80 Plasma turbulence is common in the geospace environment as well (Zimbardo et al., 2010;
81 Karimabadi et al., 2014). The geospace may be an ideal natural laboratory to study the
82 generation of turbulence in a collisionless plasma, because various regions (bow shock,
83 magnetopause, tail plasma sheet) or processes occurring there (magnetic reconnection, Kelvin-
84 Helmholtz instability (KHI), wave-particle interactions, mode conversion) can inject energy for
85 turbulence. Electromagnetic turbulence has indeed been observed in the magnetopause (e.g.,
86 LaBelle & Treumann, 1988; Rezeau & Belmont, 2001), and is suggested to be a key ingredient
87 for diffusive particle transport across the magnetopause (e.g., Johnson & Cheng, 1997; Lin et al.,
88 2012). However, the origin of electromagnetic fluctuations in the magnetopause and its boundary
89 layers remains unclear, because various processes, such as magnetopause reconnection (Chaston
90 et al., 2005), the KHI (Daughton et al., 2014; Nakamura, Hasegawa, et al., 2017), and mode
91 conversion at the magnetopause of magnetosheath compressional fluctuations (Johnson & Cheng,
92 1997; Johnson et al., 2001), can inject energy for the magnetopause turbulence.

93 In the present study, we investigate the generation process of electromagnetic turbulence in
94 magnetopause Kelvin-Helmholtz (KH) vortices by analyzing high-resolution plasma and
95 electromagnetic field data taken in situ by the Magnetospheric Multiscale (MMS) spacecraft
96 (Burch et al., 2016). For this purpose, we revisit a KH event observed by MMS on 8 September
97 2015 under northward interplanetary magnetic field (IMF) conditions. Identified in this event are
98 magnetic reconnection induced by the KHI growth because of the presence of weak but
99 significant magnetic shears across the magnetopause (Eriksson et al., 2016; Li et al., 2016;
100 Vernisse et al., 2016; Nakamura, Hasegawa, et al., 2017), turbulence in both flow and
101 electromagnetic fields and its intermittent nature (Stawarz et al., 2016), and large-amplitude
102 electrostatic waves (Wilder et al., 2016). Intermittency in the turbulence context means that
103 energy transfer across length scales is spatially nonuniform, for example with localization in
104 current sheets or filaments (e.g., Matthaeus et al., 2015). While the KHI itself could have
105 injected most energy for the turbulence as observed, it is possible that magnetopause
106 reconnection poleward of the cusp under northward IMF (e.g., Lavraud et al., 2006; Øieroset et
107 al., 2008) also played some role in the turbulence generation (Chaston et al., 2005). Indeed, in
108 the MMS KHI event, there is evidence that a prominent low-latitude boundary layer (LLBL)
109 formed through magnetopause reconnection exists on the earthward side of the KH-active
110 magnetopause (Nakamura, Eriksson, et al., 2017).

111 In this paper, the following questions are addressed. What are the relative contributions of
112 high-latitude magnetopause reconnection and the KHI to the turbulence generation in the KH
113 vortices? What is the mode of the observed electromagnetic fluctuations; are they of propagating
114 normal mode waves or something else? Could the electromagnetic turbulence play a role in
115 plasma transport across the magnetopause? Section 2 presents overviews of the MMS event on 8
116 September 2015 with both KHI and reconnection signatures and of another magnetopause event

117 with reconnection but no KHI signatures. In section 3, magnetic energy spectra are compared
 118 between the MMS observations with and without KHI signatures, and between the MMS
 119 observations and fully kinetic simulations of the KHI, to answer the question of the relative
 120 contributions. In section 4, a technique to estimate wave number vectors is used to analyze the
 121 mode of the turbulent fluctuations. In section 5, a discussion is given on the generation process
 122 of the turbulence and the causality between the turbulence and plasma transport across the
 123 magnetopause. Conclusions are provided in section 6.

124 **2 Overview of Events with and without Kelvin-Helmholtz Signatures**

125 **2.1 Kelvin-Helmholtz event on 8 September 2015**

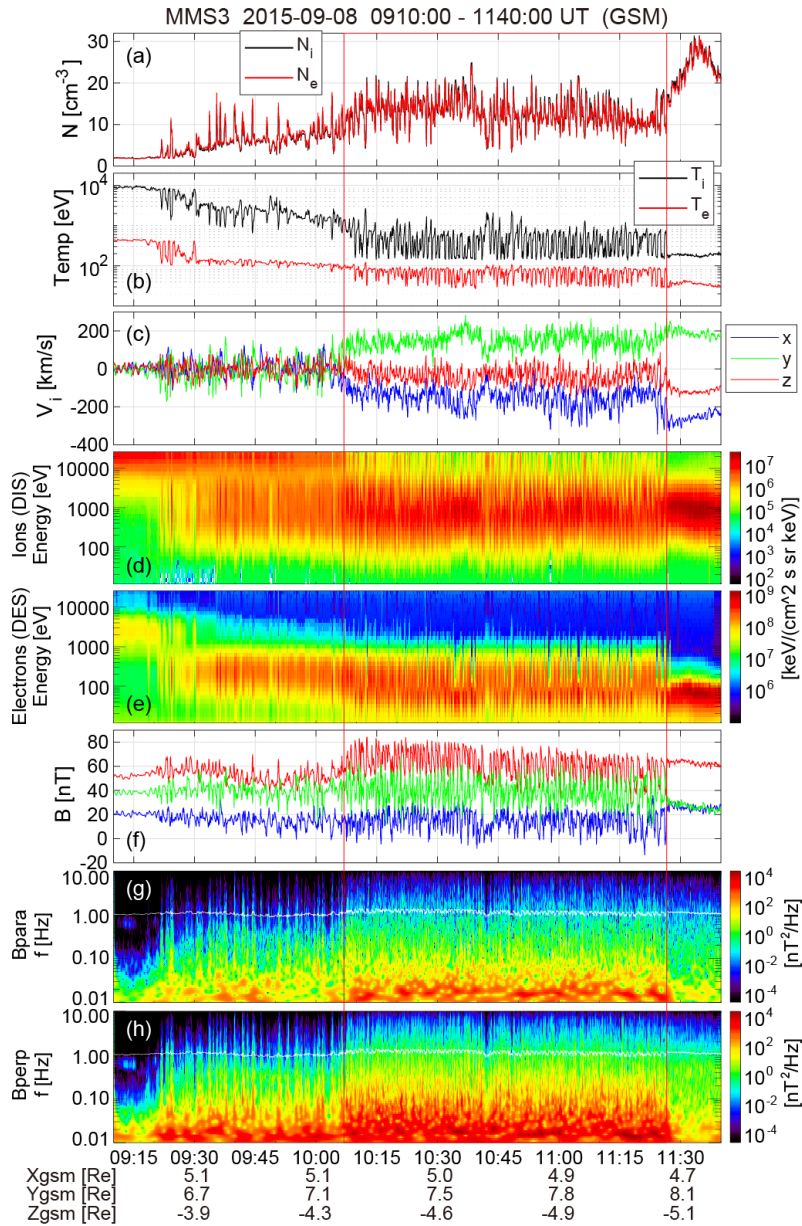
126 Figure 1 shows data of our interest, from the fluxgate magnetometer (FGM) (Russell et al.,
 127 2016) and the Fast Plasma Investigation (FPI) instrument (Pollock et al., 2016) onboard the
 128 MMS3 spacecraft for a 2.5-hour interval 0910–1140 UT on 8 September 2015, during which
 129 MMS traversed the magnetopause boundary layers from the postnoon magnetosphere into the
 130 duskside magnetosheath. On this day, an interplanetary magnetic flux rope was passing by the
 131 Earth and brought about northward IMF conditions in front of the magnetosphere (Eriksson et al.,
 132 2016). The average solar wind conditions for the interval 1030–1100 UT based on the
 133 OMNIWeb data are: IMF (B_x, B_y, B_z) = (13.2, 6.0, 14.9) in GSM, solar wind speed 506 km/s,
 134 solar wind density 10.6 cm^{-3} , plasma beta 0.15, and magnetosonic Mach number 3.7. MMS
 135 observed quasi-periodic fluctuations of the plasma bulk parameters with a period ~ 1 min
 136 (corresponding to the KHI wavelength $\sim 10^4$ km), associated with the KHI, during the interval
 137 enclosed by the red box in Figure 1 when the spacecraft were located at or near the duskside
 138 magnetopause. Based on a detailed comparison between the MMS observations and three-
 139 dimensional (3D), fully kinetic simulations of the KHI, Nakamura, Hasegawa, et al. (2017)
 140 showed that the KHI at the MMS location was in an early nonlinear phase when vortex induced
 141 reconnection (VIR) (Nakamura et al., 2011; 2013) forms jets and vortices with filamentary
 142 density structures of ion scales.

143 A dense boundary layer existed for an interval 0930–1005 UT prior to the KH-active period
 144 (Figure 1a,d). This boundary layer lacked hot magnetospheric electrons with energies ~ 5 keV,
 145 and thus likely formed through double high-latitude reconnection that can capture magnetosheath
 146 particles onto the closed portion of the dayside magnetosphere (Song & Russell, 1992; Øieroset
 147 et al., 2008). Northward increases of the boundary layer ion velocity relative to the
 148 magnetosheath flow, seen during the KH-active interval (Figure 1c), are probably due to
 149 acceleration resulting from magnetopause reconnection poleward of the southern cusp. Note that
 150 MMS was in the southern hemisphere ($z_{\text{GSM}} \sim -5 R_E$), closer to the southern than northern cusp.
 151 The presence of the dense boundary layer lowers the threshold for the KHI, and most likely
 152 made the KHI onset location closer to the subsolar point than in the case without boundary layer
 153 (Hasegawa, Retinò, et al., 2009; Nakamura, Eriksson, et al., 2017). Hereafter, this event is
 154 referred to as the RX+KHI event because both the poleward-of-the-cusp reconnection and KHI
 155 signatures were observed.

156 Low frequency fluctuations of the magnetic field were observed during the KH-active
 157 interval (Figure 1f). Large-scale variations with a quasi-period ~ 1 min (~ 0.02 Hz) are consistent
 158 with 3D deformation of field lines expected at the MMS location in the southern hemisphere
 159 through the KHI in the magnetospheric flank geometry (Hasegawa et al., 2004; Hasegawa,

160 Retinò, et al., 2009). This deformation probably allowed for KHI-induced mid-latitude
 161 reconnection (Faganello et al., 2012; Fadanelli et al., 2018), whose signatures were reported by
 162 Vernisse et al. (2016). Magnetic power spectra in Figure 1g,h show that the fluctuations are seen
 163 in the frequency range from the KHI fundamental mode (~ 0.02 Hz) to higher than the proton
 164 cyclotron frequency (~ 1 Hz). Obviously, the fluctuations during the KH-active and preceding
 165 boundary layer intervals are more intense than in the surrounding magnetosheath and
 166 magnetospheric regions, suggesting that they originated from the KHI. While considerable
 167 compressional components are present (Figure 1g), the fluctuations are dominated by the
 168 transverse components (Figure 1h).

169



170

171 **Figure 1.** MMS3 fast survey-mode observations of Kelvin-Helmholtz (KH) waves at the
 172 postnoon magnetopause on 8 September 2015 for the interval 0910–1140 UT. (a) Ion and

173 electron densities, **(b)** ion and electron temperatures assuming isotropic velocity distributions, **(c)**
 174 three GSM components of the ion velocity, **(d,e)** energy versus time spectrograms of
 175 omnidirectional ions and electrons from the dual ion spectrometer (DIS) and dual electron
 176 spectrometer (DES) parts, respectively, of the fast plasma investigation (FPI) instrument suite,
 177 **(f)** GSM components of the magnetic field, and **(g,h)** Wavelet power spectra of the magnetic
 178 field fluctuations parallel and perpendicular to the mean field, with the proton cyclotron
 179 frequency marked by the white curve. The KH-active interval 1007–1127 UT between the two
 180 vertical red lines is used to derive turbulent spectra in Figure 2.

181

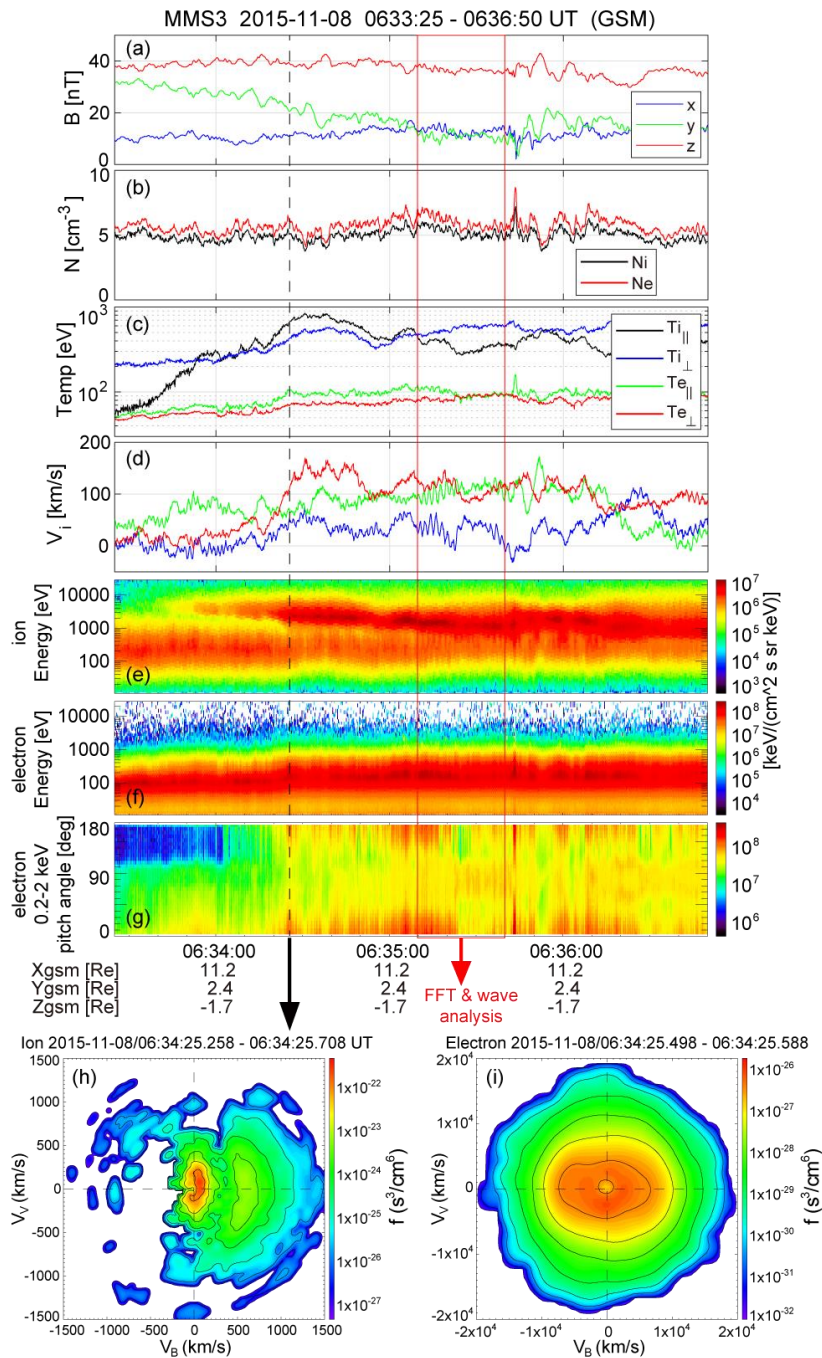
182 2.2 Subsolar magnetopause event on 8 November 2015

183 Figure 2 shows an event on 8 November 2015 when MMS traversed the subsolar
 184 magnetopause under northward IMF. The average solar wind conditions for the interval 0630–
 185 0700 UT are: IMF $(B_x, B_y, B_z) = (-8.6, 4.7, 6.0)$ in GSM, solar wind speed 478 km/s, solar
 186 wind density 2.6 cm^{-3} , plasma beta 0.12, and magnetosonic Mach number 3.2. The external
 187 conditions are thus similar to the case on 8 September 2015 in that IMF $|B_z| > |B_y|$, and the
 188 solar wind speed, beta, and Mach number are all comparable. This event, with high-latitude
 189 reconnection but without KHI signatures as demonstrated below, was selected to compare with
 190 the RX+KHI event encountered farther from the subsolar point, and to differentiate the KHI and
 191 high-latitude reconnection effects on the magnetic turbulence generation. During the interval
 192 shown in Figure 2, MMS moved from the magnetosheath into the LLBL with densities
 193 comparable to that in the magnetosheath. Because of the strong northward IMF, the
 194 magnetopause current sheet cannot be identified from the magnetic field data (Figure 2a,b)
 195 (Hasegawa, 2012). However, ion temperature increase and anisotropy variation at ~ 0634 UT
 196 from $T_{i\perp} > T_{i\parallel}$ to $T_{i\perp} \sim T_{i\parallel}$ (Figure 2c) indicate that a crossing from the magnetosheath to the
 197 LLBL occurred (Paschmann et al., 1993).

198 The observed magnetosheath boundary layer (MSBL) and LLBL had clear signatures of
 199 reconnection poleward of the southern cusp. The northward component of the ion velocity
 200 increased from near zero to ~ 100 km/s at $\sim 0634:20$ UT (Figure 2d), consistent with northward
 201 acceleration of magnetosheath ions in downstream regions equatorward of the southern cusp
 202 reconnection site. Ion velocity distributions observed in the LLBL (Figure 2h) show preexistent
 203 magnetosheath populations with $T_{i\perp} > T_{i\parallel}$ and D-shaped accelerated components with a
 204 magnetic field-aligned cutoff velocity at 300–400 km/s (Fuselier, 1995). In addition, energy
 205 dispersed ions consistent with the velocity filter effect (Figure 2e) and 0.2–2 keV electrons
 206 streaming parallel to the magnetic field, consistent with heating of magnetosheath electrons in
 207 regions southward of MMS (Figure 2g), were observed during the MSBL interval (before
 208 $\sim 0634:20$ UT). While bidirectional electron populations in the LLBL (Figure 2g,i) suggest that
 209 the magnetospheric side may be closed through double poleward-of-the-cusp reconnection
 210 (Øieroset et al., 2008), particle signatures of southern, rather than northern, cusp reconnection
 211 were prominent in the MSBL and at the magnetopause. This is probably because there was a
 212 substantial geomagnetic dipole tilt on this day and thus MMS was closer to the southern cusp,
 213 namely, the high-latitude reconnection site in the summer hemisphere (Hasegawa, McFadden, et
 214 al., 2009). This event is referred to as the RX-only event because no KHI but only reconnection
 215 signatures were identified. We note that MMS saw fluctuations of the ion velocity as well as the

216 magnetic field in the LLBL (Figure 2a,d), whose spectral properties and mode are analyzed in
 217 sections 3 and 4.

218



219

220 **Figure 2.** MMS3 burst-mode observations of a dayside, equatorial magnetopause crossing under
 221 dominantly northward IMF on 8 November 2015, 0633:25–0636:50 UT. (a) GSM components
 222 of the magnetic field, (b) ion and electron densities, (c) ion and electron temperatures in the
 223 directions parallel and perpendicular to the magnetic field, (d) GSM components of the ion
 224 velocity, (e,f) energy-time spectrograms of omnidirectional ions and electrons, (g) pitch-angle

225 distributions of 0.2–2 keV electrons, and (\mathbf{h}, \mathbf{i}) two-dimensional cuts of ion and electron velocity
 226 distributions by the plane containing the magnetic field and velocity vectors at the time marked
 227 by the vertical dashed line. The 30-sec interval enclosed by the red box is used for the spectral
 228 and \mathbf{k} -vector analyses as shown in Figures 3, 6, and 7.

229

230 3 Power Spectral Analysis

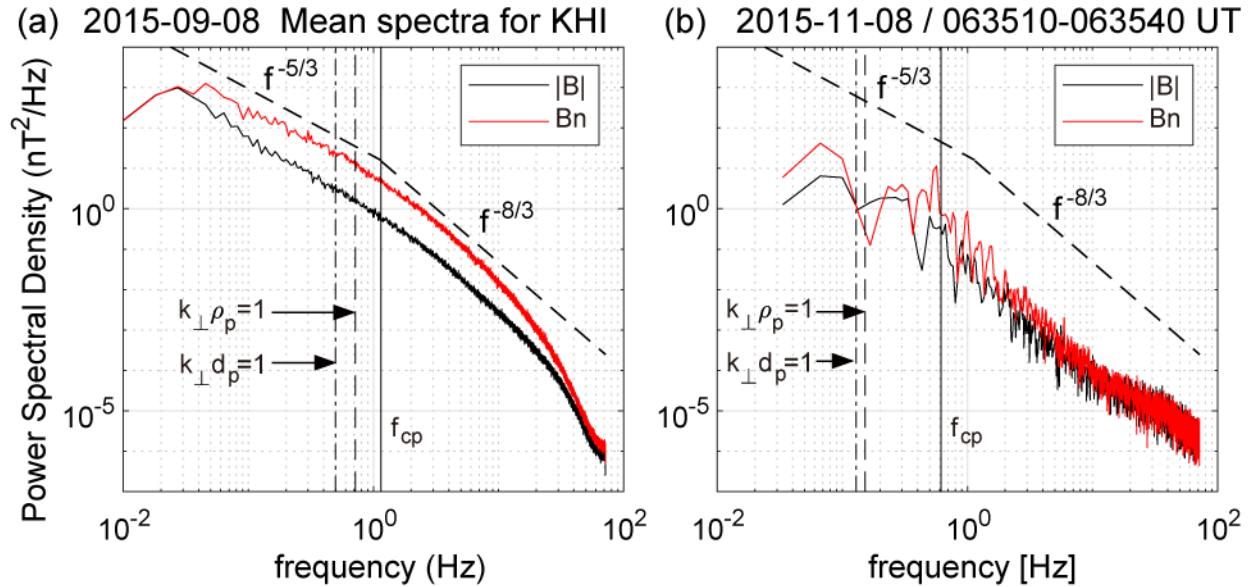
231 3.1 Comparison between the dayside reconnection and KHI events

232 Magnetic power spectra in the LLBL are compared for the RX+KHI and RX-only events in
 233 order to discuss the origin of the magnetic turbulence at magnetohydrodynamic (MHD) and ion
 234 scales observed in KH vortices. Figure 3 shows the power spectral densities (PSDs) of the field
 235 intensity $|\mathbf{B}|$ and transverse component B_n normal to the magnetopause for the two events. For
 236 the RX+KHI event, a total of 51 LLBL intervals during the KHI-active period were used to
 237 produce the mean PSDs, excluding the magnetosheath intervals and apparently reconnecting
 238 magnetopause current sheets, as reported by Eriksson et al. (2016). Here, the normal \mathbf{n} is defined
 239 to be parallel to the cross product of the mean ion velocity $\langle \mathbf{v}_i \rangle$, which is tailward roughly along
 240 the magnetopause for KH events (Hasegawa et al., 2006), and mean magnetic field $\langle \mathbf{B} \rangle$ for each
 241 interval. The frequency can be converted to the perpendicular wave number and vice versa using
 242 the Taylor hypothesis $2\pi f_{sc} = \mathbf{k}_\perp \cdot \langle \mathbf{v}_{i\perp} \rangle$, with the mean perpendicular ion velocity $\langle \mathbf{v}_{i\perp} \rangle = 204$
 243 km/s for the RX+KHI event and $\langle \mathbf{v}_{i\perp} \rangle = 76$ km/s for the RX-only event. The validity of the
 244 Taylor hypothesis will be confirmed in section 4.2. With this conversion, Figure 3 also shows the
 245 spatial scales $k_\perp \rho_p = 1$ and $k_\perp d_p = 1$, corresponding to the mean proton gyroradius $\rho_p \sim 45$ km
 246 and proton inertial length $d_p \sim 65$ km, respectively, for the RX+KHI event, and $\rho_p \sim 79$ km and
 247 $d_p \sim 94$ km for the RX-only event.

248 The PSD levels for both $|\mathbf{B}|$ and B_n are higher for the RX+KHI event than for the RX-only
 249 event for almost the entire frequency range. For comparison, we take into account the fact that
 250 the background field intensity for the RX+KHI case (~ 70 nT in Figure 1f) was about twice that
 251 for the RX-only event (~ 40 nT in Figure 2a). If the turbulence field was quasi-2D and the flux
 252 tubes in which the turbulence was embedded were advected and compressed from the subsolar
 253 location of the RX-only event to that of the RX+KHI event, the expected PSD level would be ~ 4
 254 times that seen in Figure 3b. However, the PSD of B_n is about one order of magnitude, i.e., more
 255 than four times, larger in Figure 3a than in Figure 3b. This suggests that while high-latitude
 256 reconnection can inject a modest amount of energy into turbulence at low latitudes, the KHI
 257 further amplifies the turbulence.

258 There are interesting differences in the spectral features between the RX+KHI and RX-only
 259 events. While the PSDs of $|\mathbf{B}|$ and B_n are comparable in the RX-only event, the B_n energy
 260 density is significantly higher than that of $|\mathbf{B}|$ in the RX+KHI event (Stawarz et al., 2016). At
 261 lower (MHD-scale) frequencies, the spectral index $-5/3$ for both $|\mathbf{B}|$ and B_n for the RX+KHI
 262 event is consistent with the Kolmogorov or Goldreich-Sridhar model (Goldreich & Sridhar,
 263 1995). In the higher frequency range, the index for B_n gradually decreases with frequency and
 264 becomes smaller than -3 , while that for $|\mathbf{B}|$ is in the range of -3 to $-8/3$, similar to those reported
 265 by Stawarz et al. (2016). For the RX-only event, while the fluctuations at frequencies higher than
 266 the proton cyclotron frequency f_{cp} follows $f_{sc}^{-8/3}$ for both $|\mathbf{B}|$ and B_n , the B_n spectrum only has

267 a clear peak immediately below f_{cp} . In section 4, it is shown that this intense transverse
 268 fluctuation is of electromagnetic ion-cyclotron (EMIC) waves.
 269

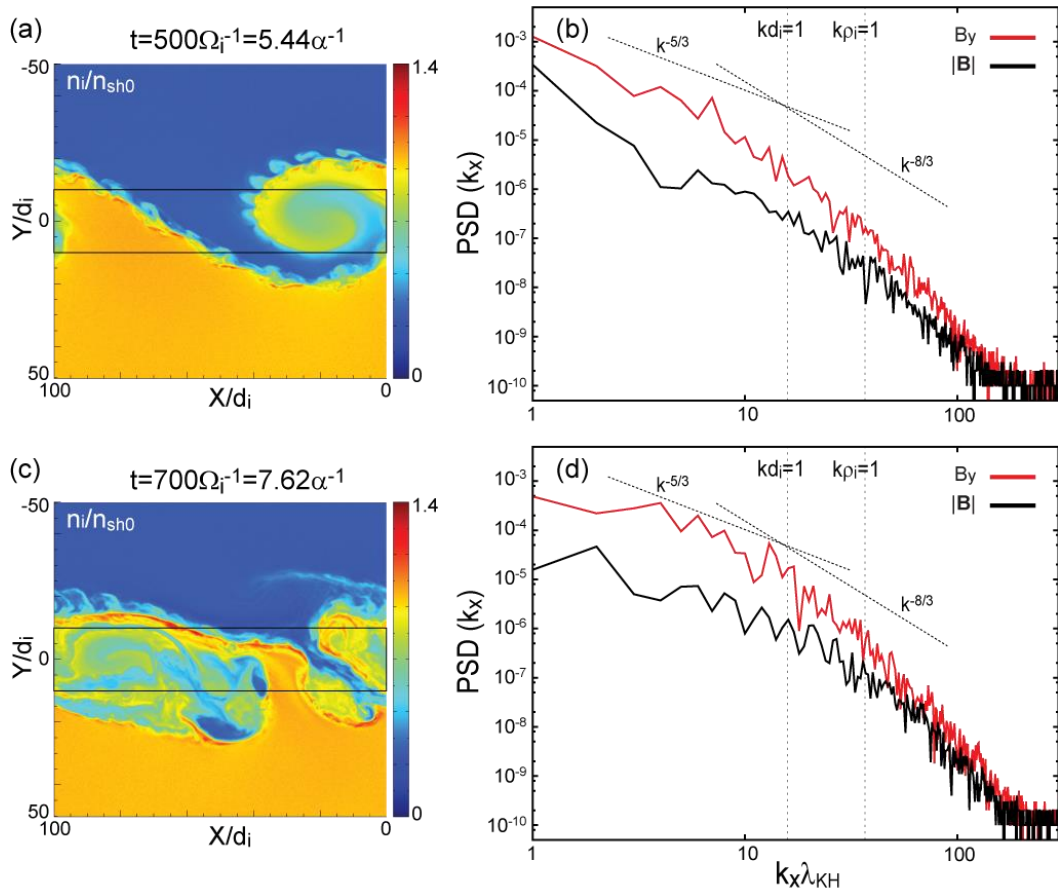


270
 271 **Figure 3.** (a) Average power spectra of the magnetic field intensity and field component
 272 perpendicular to the mean field and roughly normal to the nominal magnetopause for
 273 magnetosphere-side intervals of the KH-active period 1007–1127 UT in Figure 1. (b) Power
 274 spectra for the magnetopause boundary layer interval in Figure 2. Proton cyclotron frequency f_{cp} ,
 275 $k_{\perp}\rho_p = 1$, and $k_{\perp}d_p = 1$ are shown assuming that the observed frequency spectra are equivalent
 276 to the wave number spectra in the perpendicular direction and the Taylor hypothesis $\omega_{sc} =$
 277 $2\pi f_{sc} = \mathbf{k}_{\perp} \cdot \langle \mathbf{v}_{i\perp} \rangle$ is satisfied, where ρ_p is proton gyroradius, d_p is proton inertial length, and
 278 $\langle \mathbf{v}_{i\perp} \rangle$ is the perpendicular component of the ion bulk velocity.
 279

280 3.2 Comparison between the KHI observation and simulation

281
 282 3D fully kinetic simulations of the KHI conducted specifically for the RX+KHI event, as
 283 reported by Nakamura, Hasegawa, et al. (2017), Nakamura, Eriksson, et al. (2017), and
 284 Nakamura (2019), are compared with the MMS KHI observations in terms of spectral properties
 285 of magnetic turbulence. The initial conditions of the simulations are set based on the parameters
 286 observed in the magnetosheath- and LLBL-side regions of the KH-active magnetopause, with the
 287 initial magnetic shear $\sim 17^\circ$ and the LLBL to magnetosheath density ratio of 0.3 (see the Methods
 288 section of Nakamura, Hasegawa, et al. (2017) for details), but no broadband magnetic field or
 289 velocity fluctuations are imposed. This means that effects of turbulence that may exist in the
 290 magnetosheath and/or LLBL before the KHI onset are not included in the simulations. Figure 4
 291 shows energy spectra of $|\mathbf{B}|$ and the field component B_y normal to the initial velocity shear layer,
 292 corresponding to B_n in the MMS observations, in an early nonlinear phase ($t = 500\Omega_i^{-1}$) and
 293 more developed phase ($t = 700\Omega_i^{-1}$) of the KHI. We point out that B_y at ion to sub-ion scales
 294 roughly corresponds to reconnected field components generated by VIR (Nakamura et al., 2011;
 295 2013), though B_y at MHD scales results from large-scale evolution of KH vortices.

296 Nakamura, Hasegawa, et al. (2017) showed that the KHI in the RX+KHI event was in an
 297 early nonlinear phase, as shown in Figure 4a, when VIR was growing and formed ion-scale
 298 vortices along the interface (magnetopause) between the dense (magnetosheath) and less dense
 299 (LLBL) plasmas. At the MHD scales, the PSD of B_y is about one order of magnitude higher than
 300 that of $|\mathbf{B}|$, in agreement with the MMS observations (Figure 3a). However, the spectral index at
 301 $t = 500\Omega_i^{-1}$ is smaller than $-5/3$ seen in the observations, suggesting that the turbulence is still
 302 growing in the simulation. The observed spectral indices are rather similar to those in a more
 303 developed phase of the simulation (Figure 4d) when the plasmas are vigorously mixed within the
 304 MHD-scale vortex (Figure 4c) and the turbulence is matured. The comparison suggests that in
 305 the observed KH vortices, turbulence matured faster than in the simulation. It may be that the
 306 preexisting magnetosheath turbulence (Alexandrova et al., 2008) and/or turbulence in the LLBL
 307 generated through magnetopause reconnection (Chaston et al., 2005) contributed to faster
 308 maturation of turbulence in the observed KH vortices (T. K. M. Nakamura, private
 309 communication).
 310



311 **Figure 4.** (a,c) Density profiles in the XY plane at $t = 500\Omega_i^{-1}$ and $t = 700\Omega_i^{-1}$ from a 3D
 312 kinetic simulation of the KHI (Nakamura, 2019), where $\Omega_i = eB_0/m_i$ and $\alpha = V_0/\lambda_{KHI}$, the
 313 total velocity jump across the initial shear layer divided by the most unstable KHI wavelength.
 314 The X axis is roughly antiparallel to the initial magnetosheath flow, and the Y axis is normal to
 315 the initial velocity shear and current layers. The average wave number spectra of the magnetic
 316 energy density in normalized unit (b,d) are computed by use of the simulation data in the domain
 317 enclosed by the black boxes.
 318

319

320 **4 Dispersion Relation Analysis**

321 4.1 Bellan's method to estimate wave vectors

322 A single-spacecraft method to estimate the wave vector of magnetic field fluctuations,
 323 developed by Bellan (2012, 2016), is used to reveal the mode of the observed turbulence. The
 324 technique is based on Ampère's law and makes use of the condition that the \mathbf{k} -vector of low-
 325 frequency waves should be parallel to $\delta\mathbf{j} \times \delta\mathbf{B}$, where $\delta\mathbf{j}$ and $\delta\mathbf{B}$ are the fluctuating components
 326 of the current density and magnetic field. More exactly, wave vectors $\mathbf{k}(\omega_{sc})$ as a function of
 327 spacecraft frequency are given by

328

$$329 \quad \mathbf{k}(\omega_{sc}) = i\mu_0 \frac{\mathbf{j}(\omega_{sc}) \times \mathbf{B}^*(\omega_{sc})}{\mathbf{B}(\omega_{sc}) \cdot \mathbf{B}^*(\omega_{sc})}, \quad (1)$$

330

331 where $\mathbf{j}(\omega_{sc})$ and $\mathbf{B}(\omega_{sc})$ are the temporal Fourier transforms of the current density $\mathbf{j}(t)$ and
 332 magnetic field $\mathbf{B}(t)$, respectively, and $\mathbf{B}^*(\omega_{sc})$ is the complex conjugate of $\mathbf{B}(\omega_{sc})$ (see equation
 333 (8) of Bellan, 2016). It assumes that the displacement current is negligible, i.e., the charge quasi-
 334 neutrality is satisfied, and that there exists only one mode for a given frequency in the spacecraft
 335 frame and the fluctuations or waves are planar. While the method was first applied to MMS
 336 magnetometer measurements of $\delta\mathbf{B}$ and $\nabla \times \mathbf{B}/\mu_0$ in kinetic Alfvén waves (KAWs) propagating
 337 in a magnetopause boundary layer (Gershman et al., 2017), it can also take advantage of
 338 unprecedented high resolution ion and electron measurements by FPI that provide high cadence
 339 (30 ms) data of the current density $\mathbf{j} = ne(\mathbf{v}_i - \mathbf{v}_e)$. Applications to particle current data were
 340 made by Gershman et al. (2018) who analyzed kinetic scale turbulence in the magnetosheath.
 341 Recently, Haw et al. (2019) applied this method to identify whistler waves in a laboratory
 342 experiment of magnetic reconnection.

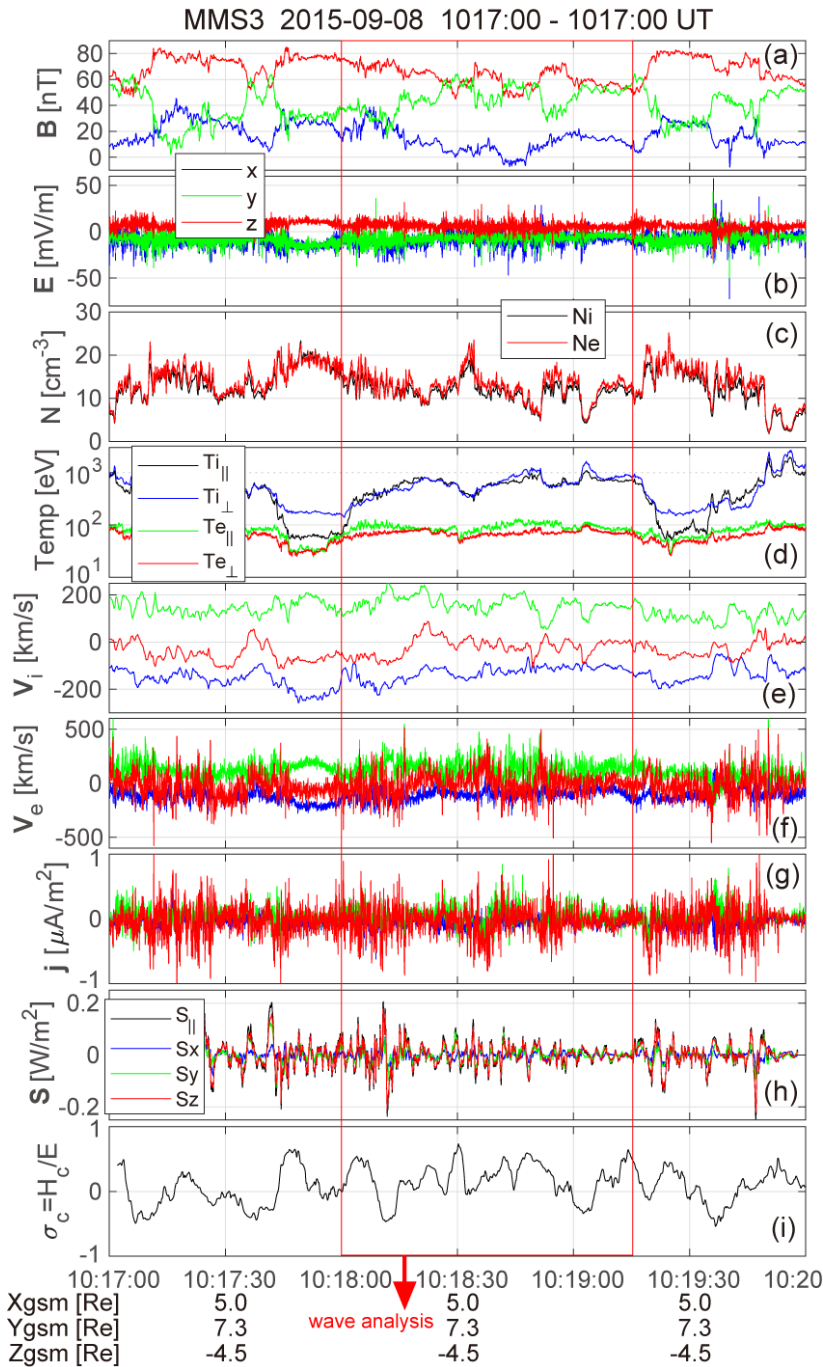
343 The method provides information similar to that obtained from the \mathbf{k} -filtering method
 344 (Pinçon & Lefeuvre, 1991) or equivalent wave telescope technique (Neubauer & Glassmeier,
 345 1990; Narita, Plaschke, et al., 2016), making use of at least four point measurements of the
 346 magnetic field. A key difference is that the \mathbf{k} -filtering and wave telescope methods permit the
 347 presence of more than one mode (\mathbf{k} -vectors) for a given frequency in the spacecraft frame. In
 348 theory, the assumption in Bellan's method of only one mode for a given frequency prohibits
 349 application to isotropic or gyrotropic turbulence in which there would be many \mathbf{k} -vectors with
 350 different directions for a given frequency. Nonetheless, Gershman et al. (2018) demonstrated that
 351 the Bellan and \mathbf{k} -filtering methods provide roughly equal wave vectors for broadband low
 352 frequency fluctuations (<3 Hz in the spacecraft frame) observed in the magnetosheath. For the
 353 RX+KHI event, the MMS spacecraft separation was ~ 175 km, much larger than the proton
 354 gyroradius ~ 45 km, so that the wave telescope or \mathbf{k} -filtering technique could not be used to
 355 analyze turbulence properties around ion scales, which are of our interest.

356 We emphasize that all the above methods do not necessarily provide wave vector(s) in the
 357 plasma rest frame, but information on the direction in which the waves or structures are
 358 propagating in the spacecraft frame. To derive the plasma-frame \mathbf{k} -vector, the Doppler effect
 359 must be taken into account. If $\mathbf{k} \cdot \mathbf{u}_0 < 0$, where \mathbf{k} is the \mathbf{k} -vector derived from the above
 360 methods and \mathbf{u}_0 is the ambient plasma flow velocity, \mathbf{k} would be the true wave vector in the
 361 plasma-rest frame. If $\mathbf{k} \cdot \mathbf{u}_0 > 0$ and the plasma frame angular frequency $\omega_{pl} = \omega_{sc} - \mathbf{k} \cdot \mathbf{u}_0 > 0$,

362 where ω_{sc} is the frequency in the spacecraft frame, the wave should be propagating along \mathbf{u}_0 and
 363 the derived \mathbf{k} -vector \mathbf{k} would be the plasma-frame wave vector, while if $\mathbf{k} \cdot \mathbf{u}_0 > 0$ and $\omega_{pl} < 0$,
 364 the true wave vector should have a component antiparallel to \mathbf{u}_0 and thus the sign of \mathbf{k} should be
 365 reversed to derive the plasma-frame wave vector (Narita et al., 2011).
 366

367 4.2 Wave vector properties

368 Figure 5 shows an example interval in the RX+KHI event to which Bellan's method is
 369 applied. We apply the method to boundary layer intervals on the magnetospheric side of the
 370 magnetopause, as marked by the red box in Figure 5, which exclude thin current sheets at the
 371 trailing edges of the KHI surface waves (Eriksson et al., 2016; Stawarz et al., 2016) and can be
 372 assumed to be of quasi-homogeneous plasma. Electric field data (Figure 5b) are from the spin-
 373 plane and axial probes measurements (Ergun et al., 2016; Lindqvist et al., 2016), and Poynting
 374 flux $\mathbf{S} = \delta\mathbf{E} \times \delta\mathbf{B}/\mu_0$ (Figure 5h) is computed in the ion-rest frame where $\delta\mathbf{E} = \mathbf{E} + \langle \mathbf{v}_i \rangle \times \langle \mathbf{B} \rangle$
 375 and $\delta\mathbf{B} = \mathbf{B} - \langle \mathbf{B} \rangle$. Here \mathbf{E} is the electric field in the spacecraft frame, and $\langle \mathbf{v}_i \rangle$ and $\langle \mathbf{B} \rangle$ are 4-sec
 376 running averages of the ion velocity and magnetic field, respectively. For the RX-only event,
 377 Bellan's method is applied to the interval 0635:10–0635:40 UT on 8 November 2015, as marked
 378 in Figure 2.
 379



380

381

382

383

384

385

386

387

388

389

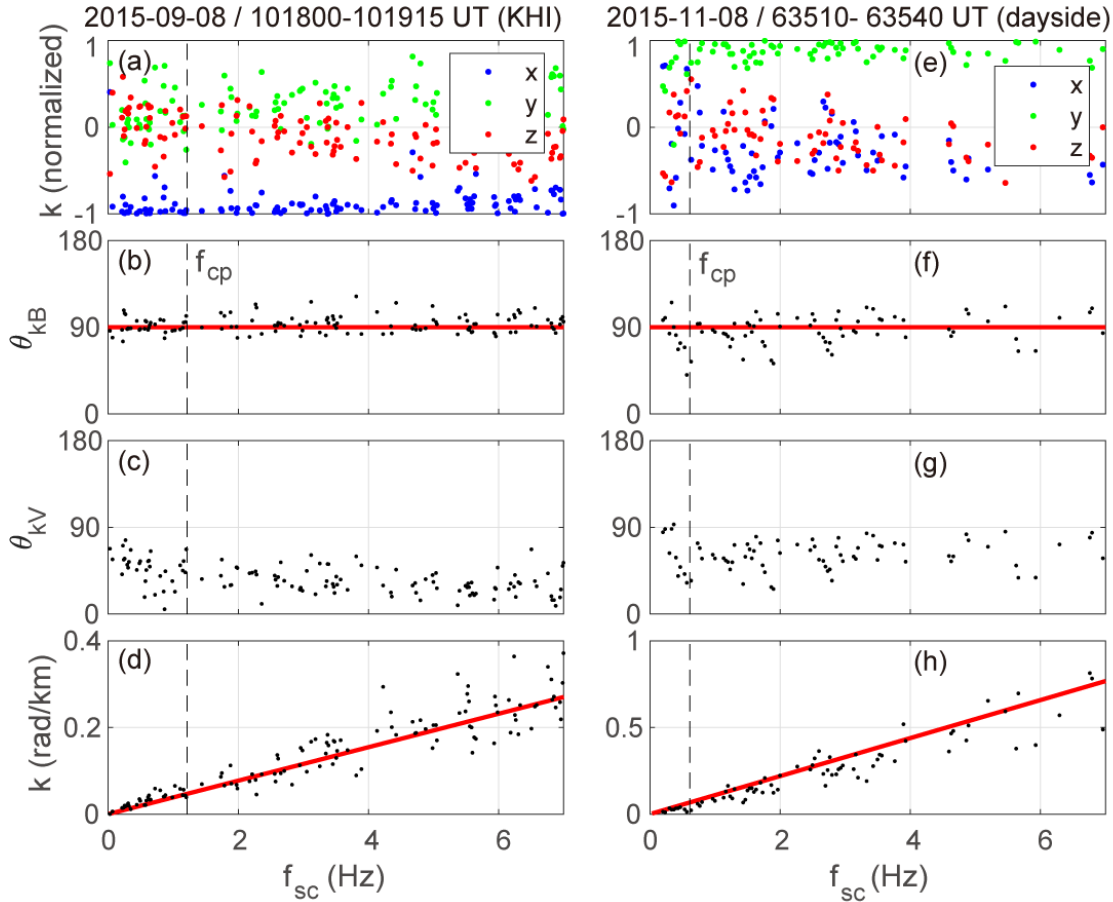
Figure 5. An example of the KH-active boundary layer intervals on 8 September 2015 used for the k-vector analysis. **(a,b)** GSM components of the magnetic and electric fields, **(c)** ion and electron densities, **(d)** ion and electron temperatures in both the parallel and perpendicular directions, **(e,f)** ion and electron velocities, and **(g)** current density based on the FPI measurements, **(h)** parallel and GSM components of Poynting flux, $\mathbf{S} = \delta\mathbf{E} \times \delta\mathbf{B}/\mu_0$, and **(i)** normalized ion cross helicities, $\sigma_c = H_c/E$, the ratio between the cross helicity and average energy (see text for details), all from the MMS3 spacecraft. The magnetosphere-side interval enclosed by the red box is used in the k-vector analysis.

390 Figure 6 shows four-spacecraft averages of the k-vector directions and the k magnitude as a
 391 function of the spacecraft frequency f_{sc} (up to 7 Hz), derived from Bellan's method, for the
 392 RX+KHI and RX-only events. A Hanning window was used when performing Fast Fourier
 393 Transforms (FFTs), following the procedure taken by Gershman et al. (2018). Figure 6 has gaps
 394 in certain frequency ranges, because the results are restricted to cases when for a given spacecraft
 395 frequency f_{sc} , the four k-vectors, derived individually for each spacecraft, all have angles less
 396 than 35° with respect to the four-spacecraft average.

397 For both the RX+KHI and RX-only events, the estimated wave vectors are nearly
 398 perpendicular to the background magnetic field (Figure 6b,f), mostly have a component along
 399 the ambient ion flow (Figure 6c,g), and roughly satisfy the Taylor hypothesis $2\pi f_{sc} =$
 400 $k\langle v_i \rangle \cos\langle \theta_{kv} \rangle$ (Figure 6d,h). The last point indicates that the turbulence fields roughly convect at
 401 the mean flow velocity, so that the spacecraft frequency f_{sc} may be converted to the wave
 402 number using the linear relation. Here, the mean field in GSM is directed along $\langle \hat{\mathbf{b}} \rangle =$
 403 $(0.160, 0.581, 0.798)$ and the mean ion velocity $\langle \mathbf{v}_i \rangle = (-132, 161, -26)$ km/s for the
 404 RX+KHI event, and $\langle \hat{\mathbf{b}} \rangle = (0.321, 0.272, 0.907)$ and $\langle \mathbf{v}_i \rangle = (31, 109, 111)$ km/s for the RX-
 405 only event. Similar features have been reported for turbulence in the solar wind (Narita et al.,
 406 2011; Sahraoui et al., 2010) and in the magnetosheath (Gershman et al., 2018). One exception is
 407 a few k-vectors at and below the proton cyclotron frequency f_{cp} for the RX-only event, which
 408 have propagation angles $\sim 45^\circ$ with respect to the magnetic field. Note that the transverse
 409 magnetic field fluctuations had a significant power around f_{cp} (Figure 3b). In section 4.3, we
 410 identify these fluctuations as of the slow (EMIC) mode.

411 To make sure that the results as shown in Figure 6 are reasonable, Bellan's method has also
 412 been applied to synthetic data taken by a virtual spacecraft passing through a simulated 3D KH
 413 vortex in a nonlinear phase, corresponding to the one shown in Figure 4c. It is found that the k-
 414 vector properties derived from the simulated data are very similar to those seen in the RX+KHI
 415 event, as shown in Figure 6a-d (see the Supporting Information). We also note that results
 416 similar to those shown in Figure 6a-d were obtained for other LLBL intervals in the RX+KHI
 417 event.

418



419
 420 **Figure 6.** Wave vector properties derived from Bellan’s method for the KH-active boundary
 421 layer interval (left: 1018:00–1019:15 UT) and dayside reconnection jet interval (right: 0635:10–
 422 0635:40 UT). (a,e) GSM components of the orientations of the \mathbf{k} -vectors, (b,f) angles between
 423 the \mathbf{k} -vectors and the mean magnetic field direction, (c,g) angles between the \mathbf{k} -vectors and the
 424 mean ion flow direction, and (d,h) the magnitude of the wave number, as a function of frequency
 425 f_{sc} in the spacecraft frame. The red line in panels (d,h) shows the Taylor condition $2\pi f_{sc} =$
 426 $k\langle v_i \rangle \cos\langle \theta_{kV} \rangle$, where $\langle v_i \rangle$ is the mean ion speed for the analysis interval and $\langle \theta_{kV} \rangle$
 427 angle between the \mathbf{k} -vectors and $\langle \mathbf{v}_i \rangle$.

428

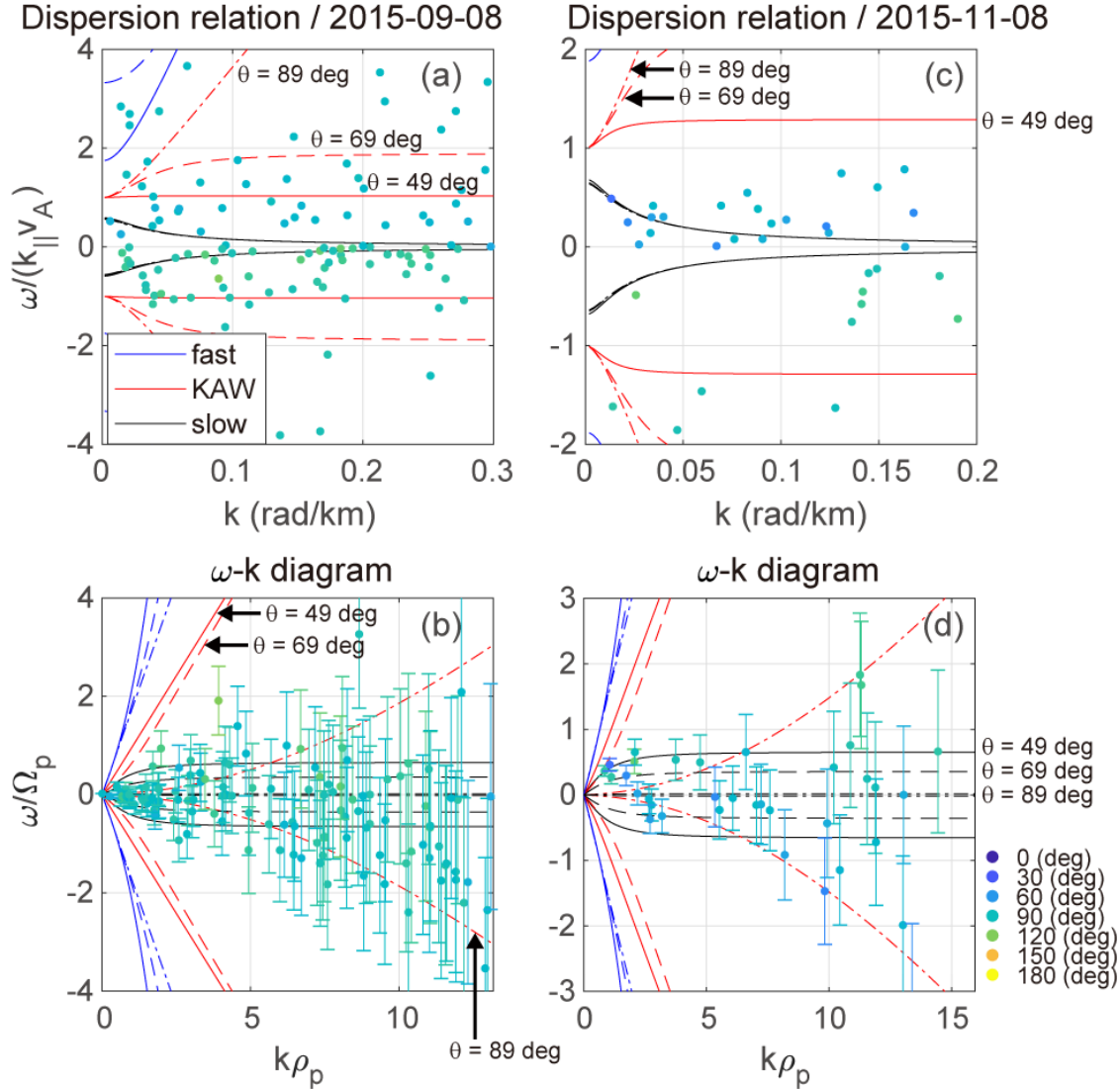
429 4.3 Dispersion relations

430 Using $\mathbf{k}(\omega_{sc})$ estimated by Bellan’s method, the dispersion relation $\omega_{pl}(\mathbf{k})$ and parallel
 431 phase velocity $\omega_{pl}(\mathbf{k})/k_{\parallel}$ in the plasma-rest frame can be derived by taking the Doppler shift
 432 into account, $\omega_{pl} = \omega_{sc} - \mathbf{k} \cdot \mathbf{u}_0$. Figure 7 shows the parallel phase velocities $\omega_{pl}(\mathbf{k})/(k_{\parallel}v_A)$
 433 normalized to the MHD Alfvén speed, and $\omega_{pl} - k$ diagrams for the two intervals, derived from
 434 the four-spacecraft averages as shown in Figure 6. Here, $v_A = 477$ km/s, $\Omega_p = eB/m_p = 7.61$
 435 rad/s, proton gyroradius $\rho_p = 44$ km, and plasma beta $\beta = 0.46$ for the RX+KHI event, and
 436 $v_A = 361$ km/s, $\Omega_p = 3.86$ rad/s, $\rho_p = 80$ km/s, and $\beta = 0.72$ for the RX-only event. The error
 437 bars in Figure 7b,d are based only on the standard deviations σ_v of the ion velocity component
 438 along \mathbf{k} during the intervals, which are ~ 60 km/s for the RX+KHI event and ~ 30 km/s for the

439 RX-only event. Error magnitudes based only on the standard deviations of the component along
440 the average ion velocity ($\langle \mathbf{v}_i \rangle = \mathbf{u}_0$) of the four k-vectors (each from each spacecraft) are
441 comparable to those in Figure 7b,d.

442 Curves in Figure 7 show theoretical linear dispersion relations for the fast (magnetosonic-
443 whistler), kinetic Alfvén, and slow (EMIC) modes based on the two-fluid model, i.e., exact
444 solutions of equation (29) derived by Bellan (2012) (see section 5 of their paper), for three
445 propagation angles $\theta = 49^\circ$, 69° , and 89° with respect to the magnetic field. For the RX+KHI
446 event, the data points are distributed around $\omega_{pl} = 0$, and do not appear to collectively satisfy
447 any of the theoretical dispersion relations. On the other hand, for the RX-only event many points
448 are near the slow-mode curve, especially at smaller k ($k < 0.1$ rad/km), while other points are
449 distributed around $\omega_{pl} = 0$. It can be concluded that the magnetic turbulence in the RX+KHI
450 event is not made of propagating normal-mode waves, but fossil magnetic field structures with
451 transverse fluctuating components were advected by the background plasma flow. On the other
452 hand, the EMIC mode was an ingredient of the fluctuations in the RX-only event.

453 We do not discuss details of the excitation process of the EMIC waves in the RX-only event,
454 which is not the focus of our study. Since they were propagating northward along the magnetic
455 field (Figure 6e,f), it is possible that they were generated closer to the reconnection site near the
456 southern cusp. We note, however, that the ion beam streaming along the magnetic field, as seen
457 in Figure 2h, would not be the driver of the waves, because EMIC waves can grow when the ion
458 beam travels in the direction opposite to the wave propagation (Ahirwar et al., 2007).
459



460
461
462
463
464
465
466
467
468
469
470
471

Figure 7. Dispersion relations derived from Bellan’s method in which the Doppler effect is subtracted for the KHI (left) and dayside reconnection (right) events. (a,c) Parallel phase velocity $\omega_{p\parallel}/(k_{\parallel}v_A)$ normalized to the Alfvén speed versus wave number, and (b,d) $\omega_{p\parallel}-k$ diagrams normalized to proton cyclotron frequency and proton gyroradius, respectively. Colors of the points denote the orientations of the k -vectors with respect to the magnetic field. Theoretical linear dispersion relations for the fast (blue), intermediate (red), and slow (black) modes are derived from equation (29) in Bellan (2012) based on the two-fluid model. Dispersion curves for three propagation angles $\theta = 49^\circ$ (solid), 69° (dashed), and 89° (dash-dot) with respect to the magnetic field are shown here. Error bars in panels (b,d) correspond to the standard deviation σ_v of the ion flow velocity component along \mathbf{k} for the analysis interval, i.e., $k\sigma_v$.

472 **5 Discussion**

473 5.1 Generation process of the KHI driven turbulence

474 Our results suggest that while magnetic reconnection at the high-latitude magnetopause
 475 excites a modest level of magnetic turbulence in the dayside low-latitude boundary layer (Figure
 476 3b), the KHI further amplifies the turbulence with the transverse magnetic energy significantly
 477 higher than the compressional energy (Figure 3a). Similar results have been obtained for
 478 simultaneous observations on 20 November 2001 of the dayside magnetopause with
 479 reconnection signatures and the dusk-flank magnetopause with active KHI signatures, reported
 480 by Hasegawa, Retinò, et al. (2009). The spectral indices $-5/3$ at MHD scales and about -3 at sub-
 481 ion scales have also been seen in other KHI events (Di Mare et al., 2019), and are consistent with
 482 2D kinetic simulations of magnetic turbulence (Franci et al., 2017) as well as 3D kinetic
 483 simulations of the KHI (Nakamura, Hasegawa, et al., 2017). The transverse components of sub-
 484 ion-scale magnetic field fluctuations roughly corresponds to the reconnected field components
 485 and, notably, both kinetic simulations and observations show that magnetic reconnection can
 486 produce magnetic turbulence with the spectral index of about $-8/3$ at sub-ion scales (Daughton et
 487 al., 2014; Eastwood et al., 2009), consistent with the present observations.

488 It should be stressed that power-law magnetic spectra with a spectral index $-5/3$ in the MHD
 489 range, as expected for a quasi-steady turbulence, were observed even in the early nonlinear phase
 490 (at $1-2$ eddy turnover time $\pi\alpha^{-1} = \pi\lambda_{\text{KHI}}/V_0$) of the KHI, corresponding to the stage as shown
 491 in Figure 4a. What could be the process for such fast turbulence generation? Recent kinetic
 492 simulations of the KHI show that if modest magnetic field fluctuations, as seen in Figure 3b, are
 493 present in the magnetopause before the KHI onset, magnetic turbulence with a spectral index $-$
 494 $5/3$ can be generated even in the early nonlinear stage (T. K. M. Nakamura, private
 495 communication, 2019).

496 We also note that energy cascade in KH vortices may be proceeding through the process, as
 497 suggested by Franci et al. (2017), in which magnetic reconnection may act as a rectifier to
 498 directly transfer energy from MHD scales to sub-ion scales, rapidly driving sub-ion-scale energy
 499 cascade. In such situations, energy injected at MHD scales can be transferred to smaller scales
 500 not only gradually via standard direct cascade but also rapidly via reconnection that occurs in
 501 sub-ion-scale current sheets. Their results are interesting in that cross-scale energy transfer in
 502 turbulence may occur via magnetic reconnection (see Figure 4 of Franci et al., 2017), while
 503 conventional wisdom is that energy cascade at MHD scales occurs via nonlinear interactions of
 504 vortices or counter-propagating Alfvén waves. In the case of the KHI with an initial magnetic
 505 shear or magnetic field deformation involved (Nakamura et al., 2006; Nykyri & Otto, 2001),
 506 MHD dynamics (vortical flow) produces thin current sheets subject to magnetic reconnection
 507 and, as a result of VIR, part of energy at MHD scales may be directly transferred to sub-ion
 508 scales, and forward and inverse cascades at kinetic scales may set in.

509

510 5.2 Mode of the KHI driven turbulence

511 The nature of electromagnetic field fluctuations in KH vortices is discussed in detail. The
 512 analysis in section 4 suggests that the magnetic turbulence in KH vortices does not satisfy any
 513 linear dispersion relation for propagating normal-mode waves, and thus consists of magnetic
 514 structures of various scales being advected by the background bulk flow ($\omega_{\text{pl}} \sim 0$). The k -vectors
 515 roughly perpendicular to the background field (Figure 6b) indicates that the magnetic structures

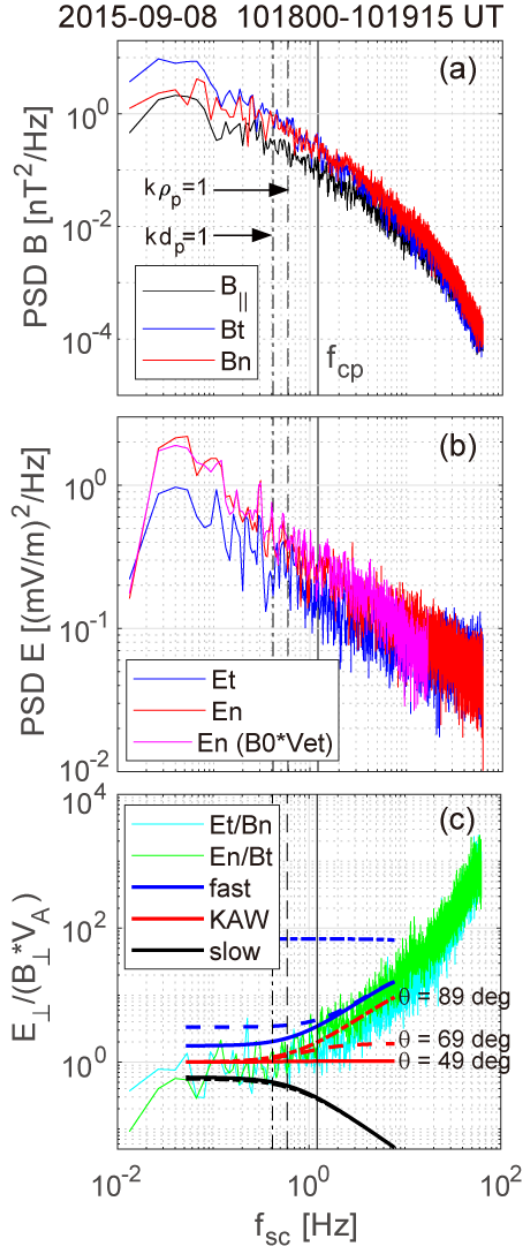
516 with transverse field fluctuations (Figure 3a) have boundaries or inhomogeneity roughly in the
 517 perpendicular direction, i.e., the turbulence consists of weakly curved magnetic flux tubes of
 518 various scales. We note that such flux tubes can be produced in KH vortices through multiple
 519 VIR and become interlaced in the nonlinear phase (see Figure 6 of Nakamura et al. (2013)). Such
 520 a filamentary or “spaghetti-like” flux tubes picture has been suggested and demonstrated for
 521 turbulence in the solar wind (Borovsky, 2008; Hu et al., 2018), at least part of which would be
 522 driven by convective fluid motions on the photosphere.

523 A caveat is that the assumptions underlying Bellan’s method of plane waves or planar
 524 structures and one mode for a given spacecraft frequency may well be violated in KH vortices.
 525 Indeed, Figure 5h,i shows that both Poynting flux and the normalized cross helicity, the latter of
 526 which can be used as a measure of Alfvénicity of MHD turbulence and to infer the propagation
 527 direction in the plasma frame of Alfvén waves, intermittently have significant positive or
 528 negative values during the analyzed and other intervals. It suggests that counter-propagating
 529 Alfvén waves may be embedded in KH vortices. Here, the normalized ion cross helicity is
 530 defined as $\sigma_{ci} = H_{ci}/E_i$, where the ion cross helicity $H_{ci} = \langle \mathbf{v}_i \cdot \mathbf{b} \rangle$, average energy $E_i =$
 531 $\langle v_i^2 + b^2 \rangle / 2$, and the magnetic field \mathbf{b} is expressed in Alfvén units $\mathbf{B} / \sqrt{\mu_0 \rho_p}$ (Bruno & Carbone,
 532 2013).

533 With the possibility of counter-propagating waves in mind, we have analyzed energy spectra
 534 of electric field fluctuations and the ratio between the normal component of the fluctuating
 535 electric field and the tangential component of the fluctuating magnetic field, as shown in Figure
 536 8. Here the normal is $\mathbf{n} = (0.705, 0.499, -0.504)$ in GSM, and the tangential direction is
 537 defined as $\mathbf{t} = \langle \hat{\mathbf{b}} \rangle \times \mathbf{n} = (-0.691, 0.643, -0.330)$. The ratio is equivalent to the parallel phase
 538 velocity of the waves, when the wave vectors are in the plane containing $\langle \hat{\mathbf{b}} \rangle$ and \mathbf{t} . This may
 539 well be the case because the k-vectors from Bellan’s method are roughly along the mean flow
 540 velocity \mathbf{u}_0 which is in the $\langle \hat{\mathbf{b}} \rangle - \mathbf{t}$ plane (Figure 6b,c). Here, the measured electric field is
 541 converted to that in the mean flow frame, $\mathbf{E}' = \mathbf{E} + \mathbf{u}_0 \times \mathbf{B}$. Figure 8b shows that the transverse
 542 component of \mathbf{E}' is dominated by that $-\delta \mathbf{v}_e \times \mathbf{B}_0$, which is because the amplitude of the
 543 magnetic field fluctuations $\delta \mathbf{B}$ during the boundary layer interval is considerably smaller than
 544 $|\mathbf{B}_0|$ (Figure 5a).

545 The amplitude of δE_n being larger than that of δE_t may be due to electron jets from VIR
 546 being roughly directed in the tangential direction, i.e., $|\delta v_{et}|$ larger than $|\delta v_{en}|$. Interestingly,
 547 Figure 8c shows that both $\delta E_n / \delta B_t$ and $\delta E_t / \delta B_n$ roughly satisfy the linear dispersion relation of
 548 KAWs with $\theta = 89^\circ$, the propagation angle compatible with the observed k-vector directions
 549 (Figure 6b), and using the Taylor hypothesis. This may indicate that KAWs were a constituent of
 550 the electromagnetic turbulence observed in the KH vortices. However, $|\delta E_n| > |\delta E_t|$ (Figure 8b)
 551 suggests that the wave vectors had larger normal, rather than tangential, components if KAWs
 552 are involved (Hollweg, 1999; Bellan, 2012; Lin et al., 2012). In fact, if KAWs are emitted by
 553 VIR, it is reasonable to suppose that the wave vectors point mostly in the normal, rather than
 554 tangential, direction, as in the case of MHD Alfvén waves (rotational discontinuities) emitted
 555 from reconnecting current sheets. We also point out that the KAW modes with wave vectors
 556 mostly along the normal cannot simply result from mode conversion from the KH waves
 557 (Chaston et al., 2007), because KH waves have wave vectors roughly in the tangential direction.

558



559
 560 **Figure 8.** (a) Power spectra of the magnetic field components parallel and perpendicular to the
 561 mean magnetic field. The perpendicular components δB_n and δB_t are roughly normal and
 562 tangential, respectively, to the magnetopause. (b) Power spectra of the electric field components
 563 δE_n and δE_t perpendicular to the mean magnetic field in the mean flow frame. The magenta line
 564 shows the spectrum of the normal component of the convection electric field $\mathbf{E}_c = -\mathbf{v}_{e\perp} \times \mathbf{B}_0$.
 565 (c) $\delta E_t/\delta B_n$ (cyan) and $\delta E_n/\delta B_t$ (green), normalized to the Alfvén speed. The curves show
 566 linear dispersion relations based on the two-fluid model (Bellan, 2012) of fast, intermediate
 567 (KAW), and slow mode waves for three propagation angles $\theta = 49^\circ$ (solid), 69° (dashed), and
 568 89° (dash-dot) with respect to the background magnetic field.

569
 570 How could these seemingly contradictory results be reconciled? One possibility is that the
 571 electromagnetic fluctuations in the KH vortices are in a strongly turbulent state, and thus do not

572 satisfy the properties of linear modes, such as linear dispersion relations. It is also possible that
 573 since magnetic reconnection can excite KAWs in outflow regions (Chaston et al., 2005) and VIR
 574 in 3D can occur at various latitudinal locations (Vernisse et al., 2016; Nakamura, Hasegawa, et
 575 al., 2017; Nakamura, Eriksson, et al., 2017; Fadanelli et al., 2018), KAWs propagating in
 576 opposite directions are embedded and interacting in the KH vortices. Indeed, magnetic flux ropes
 577 observed in association with the KH-active magnetopause (Eriksson et al., 2009; Sturmer et al.,
 578 2018) are signatures of such multiple reconnection in KH vortices, and may actually be
 579 interlaced flux tubes in 3D. Notably, the interlaced field lines with filamentary currents in the
 580 KH vortices may be the origin of intermittent features of the turbulence, as reported by Stawarz
 581 et al. (2016). We also point out that the presence of positive and negative ω_{pl} (Figure 7a,b) may
 582 be interpreted as a signature of waves/structures having k-vector components parallel and
 583 antiparallel to \mathbf{u}_0 in the plasma-rest frame. However, since the FFT-based Bellan method allows
 584 only one mode for a given spacecraft frequency and selected interval, the turbulence as a whole
 585 may manifest as magnetic structures advected by the bulk flow in the KH vortices. Future studies
 586 using Bellan's method should probably use more advanced spectral analysis, such as wavelet
 587 transforms, to derive instantaneous wave vectors.

588 The possibility that VIR could excite KAWs indicates that there may be a new path to locally
 589 generate KAW turbulence in the magnetopause boundary layer, in addition to the paths through
 590 dayside magnetopause reconnection (Chaston et al., 2005) and resonant mode conversion from
 591 magnetopause surface or KH waves (Hasegawa, 1976; Chaston et al., 2007) or from
 592 magnetosheath compressional waves (Johnson & Cheng, 1997; Lin et al., 2010). The role of such
 593 VIR driven KAWs is unknown and needs to be explored in the future.

594

595 5.3 Role of the KHI driven turbulence

596 Earlier observations demonstrated that magnetic reconnection can be induced locally at the
 597 KH-unstable magnetopause and remotely at mid-latitudes as a consequence of the KHI (Eriksson
 598 et al., 2016; Nakamura, Hasegawa, et al., 2017; Vernisse et al., 2016). Simulation studies
 599 (Nakamura, Hasegawa, et al., 2017; Nakamura, Eriksson, et al., 2017) also show that VIR in 3D
 600 can cause an efficient plasma mixing and drive magnetic turbulence with a power-law index $-8/3$
 601 at sub-ion scales as observed. Combined with such results, our results suggest that the sub-ion-
 602 scale turbulence in the early nonlinear phase of the KHI is a consequence of VIR, the primary
 603 plasma transport process at this stage.

604 If KAW turbulence could be excited through VIR (Figure 8c), one may think that particle
 605 diffusion induced by KAWs could play an additional role in the transport across the
 606 magnetopause (Johnson & Cheng, 1997; Izutsu et al., 2012), in particular if the KAW turbulence
 607 is further amplified in more downstream regions. However, the KAW mode with $|\delta E_n| > |\delta E_t|$
 608 (Figure 8b) does not significantly contribute to such transport, which may be observationally
 609 confirmed by a methodology developed by Izutsu et al. (2012). Thus, the mode with $|\delta E_n| >$
 610 $|\delta E_t|$ first needs to be converted through a parametric decay instability to the one with $|\delta E_n| \leq$
 611 $|\delta E_t|$ for massive transport to be realized (Lin et al., 2012). Besides such a nonlinear mode
 612 conversion and likely ongoing Landau and transit damping of KAWs, whereby ions and
 613 electrons may be heated and undergo cross-field diffusion (Johnson & Cheng, 2001; Chaston et
 614 al., 2008; Wang et al., 2019), there may be a competition between possible amplification of
 615 KAWs via an inverse cascade (vortex merging) (Miura, 1997) and damping by the resistive
 616 ionosphere (Borovsky & Funsten, 2003) to which LLBL field lines are connected. These

617 processes expected farther down the tail should be investigated in the future both observationally
618 and numerically, in addition to the effects of eddy diffusion associated with flow velocity
619 fluctuations (Matsumoto & Hoshino, 2004; Wang et al., 2010), in order to understand the
620 formation process of the dense plasma sheet observed under northward IMF conditions (Wing et
621 al., 2005).
622

623 **6 Conclusions**

624 We have investigated the generation process and mode properties of electromagnetic
625 turbulence observed in KH vortices encountered at the dusk-flank magnetopause by the MMS
626 spacecraft on 8 September 2015 under northward IMF conditions. The event on this day was
627 compared with another MMS event under a similar solar wind and IMF condition in which
628 magnetopause reconnection signatures but no KHI signatures were observed at the dayside
629 magnetopause. We found that while high-latitude reconnection can excite a modest level of
630 turbulence in the dayside low-latitude boundary layer, the KHI significantly enhances the
631 turbulence level even in its early nonlinear phase, leading to magnetic energy spectra with
632 power-law indices of about $-5/3$ at MHD scales and about $-8/3$ at sub-ion scales. Our wave
633 vector and dispersion relation analysis suggests that the turbulence consists of interlaced
634 magnetic flux tubes of various scales advected by plasma flows in the KH vortices, rather than of
635 propagating normal mode waves. Combined with the evidence reported earlier for vortex
636 induced reconnection (VIR) in the present MMS event (Eriksson et al., 2016; Li et al., 2016;
637 Vernisse et al., 2016) and the results from 3D fully kinetic simulations that VIR in 3D can
638 produce interlaced reconnected field lines, cause an efficient plasma mixing, and generate
639 power-law magnetic energy spectra with a spectral index $-8/3$ at sub-ion scales (Nakamura,
640 Hasegawa, et al., 2017; Nakamura, Eriksson, et al., 2017), we conclude that the sub-ion scale
641 turbulence in the early nonlinear phase is not the primary cause of the plasma transport across the
642 magnetopause, but a consequence of 3D VIR.
643

644 **Acknowledgments**

645 The MMS data used here are available from the MMS Science Data Center:
646 <https://lasp.colorado.edu/mms/sdc/public/>. The analyses presented used version 3.3 of the FPI
647 burst-mode data. Data access and processing was done using SPEDAS V3.1 (Angelopoulos et al.,
648 2019). We thank Natalia Papatashvili at the National Space Science Data Center (NSSDC) of
649 NASA/GSFC for the use of the OMNI 2 data set (OMNI data from
650 <http://omniweb.gsfc.nasa.gov/>). For the simulation analyzed in this paper, we acknowledge
651 PRACE for awarding us access to MareNostrum at Barcelona Supercomputing Center (BSC),
652 Spain. An IDL code of the method to estimate the k-vectors used here is included in the
653 Supporting Information of Bellan (2016), and a corresponding Matlab code is included in the
654 Supporting Information of the present paper. H.H. thanks Tony Lui, Yasuhito Narita, Luca
655 Sorriso-Valvo, and Nobumitsu Yokoi for inspiring discussion.

656 **References**

657 Ahirwar, G., Varma, P., & Tiwari, M. S. (2007). Beam effect on electromagnetic ion-cyclotron
658 waves with general loss-cone distribution function in an anisotropic plasma-particle
659 aspect analysis. *Ann. Geophys.*, 25, 557-568. <https://doi.org/10.5194/angeo-25-557-2007>

- 660 Alexandrova, O., Lacombe, C., & Mangeney, A. (2008). Spectra and anisotropy of magnetic
661 fluctuations in the Earth's magnetosheath: Cluster observations. *Ann. Geophys.*, 26,
662 3585-3596. <https://doi.org/10.5194/angeo-26-3585-2008>
- 663 Alexandrova, O., Saur, J., Lacombe, C., Mangeney, A., Mitchell, J., Schwartz, S. J., & Robert, P.
664 (2009). Universality of solar-wind turbulence spectrum from MHD to electron scales,
665 *Phys. Rev. Lett.*, 103, 165003. <https://doi.org/10.1103/PhysRevLett.103.165003>
- 666 Alexandrova, O., Chen, C. H. K., Sorriso-Valvo, L., Horbury, T. S., & Bale, S. D. (2013). Solar
667 wind turbulence and the role of ion instabilities. *Space Sci. Rev.*, 178, 101-139.
668 doi:10.1007/s11214-013-0004-8
- 669 Angelopoulos, V., Cruce, P., Drozdov, A., Grimes, E. W., et al. (2019). The Space Physics
670 Environment Data Analysis System (SPEDAS). *Space Sci. Rev.*, 215, 9.
671 <https://doi.org/10.1007/s11214-018-0576-4>
- 672 Balbus, S. A., & Hawley, J. F. (1998). Instability, turbulence, and enhanced transport in
673 accretion disks. *Rev. Modern Phys.*, 70, 1-53. <https://doi.org/10.1103/RevModPhys.70.1>
- 674 Bellan, P. M. (2012). Improved basis set for low frequency plasma waves. *J. Geophys. Res.*, 117,
675 A12219. doi:10.1029/2012JA017856
- 676 Bellan, P. M. (2016). Revised single-spacecraft method for determining wave vector k and
677 resolving space-time ambiguity. *J. Geophys. Res. Space Physics*, 121, 8589-8599.
678 doi:10.1002/2016JA022827
- 679 Borovsky, J. E., & Funsten, H. O. (2003). MHD turbulence in the Earth's plasma sheet:
680 Dynamics, dissipation, and driving. *J. Geophys. Res.*, 108, 1284.
681 doi:10.1029/2002JA009625
- 682 Borovsky, J. E. (2008). Flux tube texture of the solar wind: Strands of the magnetic carpet at 1
683 AU? *J. Geophys. Res.*, 113, A08110. doi:10.1029/2007JA012684
- 684 Bruno, R., & Carbone, V. (2013). The solar wind as a turbulence laboratory. *Living Rev. Solar*
685 *Phys.*, 10, 2. doi:10.12942/lrsp-2013-2
- 686 Burch, J. L., Moore, T. E., Torbert, R. B., & Giles, B. L. (2016). Magnetospheric Multiscale
687 overview and science objectives. *Space Sci. Rev.*, 199, 5-21. doi:10.1007/s11214-015-
688 0164-9
- 689 Chaston, C. C., Phan, T. D., Bonnell, J. W., Mozer, F. S., Acuna, M., Goldstein, M. L., Balogh,
690 A., André, M., Rème, H., & Fazakerley, A. (2005). Drift-kinetic Alfvén waves observed
691 near a reconnection X line in the Earth's magnetopause. *Phys. Rev. Lett.*, 95, 065002.
692 <https://doi.org/10.1103/PhysRevLett.95.065002>
- 693 Chaston, C. C., Wilber, M., Mozer, F. S., Fujimoto, M., Goldstein, M. L., Acuna, M., Rème, H.,
694 & Fazakerley, A. (2007). Mode conversion and anomalous transport in Kelvin-Helmholtz
695 vortices and kinetic Alfvén waves at the Earth's magnetopause. *Phys. Rev. Lett.*, 99,
696 175004. <https://doi.org/10.1103/PhysRevLett.99.175004>
- 697 Chaston, C., Bonnell, J., McFadden, J. P., et al. (2008). Turbulent heating and cross-field
698 transport near the magnetopause from THEMIS. *Geophys. Res. Lett.*, 35, L17S08.
699 doi:10.1029/2008GL033601

- 700 Chen, C. H. K. (2016). Recent progress in astrophysical plasma turbulence from solar wind
 701 observations. *J. Plasma Phys.*, 82, 535820602.
 702 <https://doi.org/10.1017/S0022377816001124>
- 703 Daughton, W., Nakamura, T. K. M., Karimabadi, H., Roytershteyn, V., & Loring, B. (2014).
 704 Computing the reconnection rate in turbulent kinetic layers by using electron mixing to
 705 identify topology. *Phys. Plasmas*, 21, 052307. doi:10.1063/1.4875730
- 706 Di Mare, F., Sorriso-Valvo, L., Retinò, A., Malara, F., & Hasegawa, H. (2019). Evolution of
 707 turbulence in the Kelvin-Helmholtz instability in the terrestrial magnetopause.
 708 *Atmosphere*, 10(9), 561. <https://doi.org/10.3390/atmos10090561>
- 709 Eastwood, J. P., Phan, T. D., Bale, S. D., & Tjulin, A. (2009). Observations of turbulence
 710 generated by magnetic reconnection. *Phys. Rev. Lett.*, 102, 035001.
 711 doi:10.1103/PhysRevLett.102.035001
- 712 Ergun, R. E., Tucker, S., Westfall, J., et al. (2016). The axial double probe and fields signal
 713 processing for the MMS mission. *Space Sci. Rev.*, 199, 167-188. doi:10.1007/s11214-
 714 014-0115-x
- 715 Eriksson, S., Hasegawa, H., Teh, W.-L., et al. (2009). Magnetic island formation between large-
 716 scale flow vortices at an undulating postnoon magnetopause for northward interplanetary
 717 magnetic field. *J. Geophys. Res.*, 114, A00C17. doi:10.1029/2008JA013505
- 718 Eriksson, S., Lavraud, B., Wilder, F. D., et al. (2016). Magnetospheric Multiscale observations
 719 of magnetic reconnection associated with Kelvin-Helmholtz waves. *Geophys. Res. Lett.*,
 720 43, 5606-5615. doi:10.1002/2016GL068783
- 721 Fadanelli, S., Faganello, M., Califano, F., Cerri, S. S., Pegoraro, F., & Lavraud, B. (2018).
 722 North-south asymmetric Kelvin-Helmholtz instability and induced reconnection at the
 723 Earth's magnetospheric flanks. *Journal of Geophysical Research: Space Physics*, 123.
 724 <https://doi.org/10.1029/2018JA025626>
- 725 Faganello, M., Califano, F., Pegoraro, F., & Andreussi, T. (2012). Double mid-latitude
 726 dynamical reconnection at the magnetopause: An efficient mechanism allowing solar
 727 wind to enter the Earth's magnetosphere. *Europhys. Lett.*, 100(6), 69001,
 728 doi:10.1209/0295-5075/100/69001
- 729 Fox, N. J., Velli, M. C., Bale, S. D., Decker, R., Driesman, A., Howard, R. A., Kasper, J. C.,
 730 Kinnison, J., Kusterer, M., Lario, D., Lockwood, M. K., McComas, D. J., Raouafi, N. E.,
 731 & Szabo, A. (2016). The Solar Probe Plus mission: Humanity's first visit to our star.
 732 *Space Sci. Rev.*, 204, 7-48. <https://doi.org/10.1007/s11214-015-0211-6>
- 733 Franci, L., Cerri, S. S., Califano, F., et al. (2017). Magnetic reconnection as a driver for a sub-
 734 ion-scale cascade in plasma turbulence. *Astrophys. J. Lett.*, 850, L16. doi:10.3847/2041-
 735 8213/aa93fb
- 736 Fuselier, S. A. (1995). Kinetic aspects of reconnection at the magnetopause. in *Physics of the*
 737 *Magnetopause*, edited by P. Song, B. U. Ö. Sonnerup, and M. F. Thomsen, pp.181–187,
 738 AGU, Washington, D. C. doi 10.1029/GM090p0181
- 739 Gaensler, B. M., Haverkorn, M., Burkhart, B., Newton-McGee, K. J., Ekers, R. D., Lazarian, A.,
 740 McClure-Griffiths, N. M., Robishaw, T., Dickey, J. M., & Green, A. J. (2011). Low-

- 741 Mach-number turbulence in interstellar gas revealed by radio polarization gradients.
742 Nature, 478, 214-217. doi:10.1038/nature10446
- 743 Gershman, D. J., F-Vinas, A., Dorelli, J. C., et al. (2017). Wave-particle energy exchange
744 directly observed in a kinetic Alfvén-branch wave. Nature Communications, 8, 14719.
745 doi:10.1038/ncomms14719
- 746 Gershman, D. J., F-Vinas, A., Dorelli, J. C., et al. (2018). Energy partitioning constraints at
747 kinetic scales in low-beta turbulence. Phys. Plasmas, 25, 022303.
748 <https://doi.org/10.1063/1.5009158>
- 749 Goldreich, P., & Sridhar, S. (1995). Toward a theory of interstellar turbulence. 2: Strong
750 Alfvénic turbulence. Astrophys. J., 438, 763-775. doi:10.1086/175121
- 751 Hasegawa, A. (1976). Particle acceleration by MHD surface wave and formation of aurora. J.
752 Geophys. Res., 81, 5083-5090. doi:10.1029/JA081i028p05083
- 753 Hasegawa, H. (2012). Structure and dynamics of the magnetopause and its boundary layers.
754 Monogr. Environ. Earth Planets, 1(2), 71-119, doi:10.5047/meep.2012.00102.0071
- 755 Hasegawa, H., Fujimoto, M., Phan, T.-D., Rème, H., Balogh, A., Dunlop, M. W., ... TanDokoro,
756 R. (2004). Transport of solar wind into Earth's magnetosphere through rolled-up Kelvin-
757 Helmholtz vortices. Nature, 430, 755-758. <https://doi.org/10.1038/nature02799>
- 758 Hasegawa, H., Fujimoto, M., Takagi, K., Saito, Y., Mukai, T., & Rème, H. (2006). Single-
759 spacecraft detection of rolled-up Kelvin-Helmholtz vortices at the flank magnetopause. J.
760 Geophys. Res., 111, A09203. doi:10.1029/2006JA011728
- 761 Hasegawa, H., McFadden, J. P., Constantinescu, O. D., et al. (2009). Boundary layer plasma
762 flows from high-latitude reconnection in the summer hemisphere for northward IMF:
763 THEMIS multi-point observations. Geophys. Res. Lett., 36, L15107.
764 doi:10.1029/2009GL039410
- 765 Hasegawa, H., Retinò, A., Vaivads, A., Khotyaintsev, Y., André, M., Nakamura, T. K. M., Teh,
766 W.-L., Sonnerup, B. U. Ö., Schwartz, S. J., Seki, Y., Fujimoto, M., Saito, Y., Rème, H.,
767 & Canu, P. (2009). Kelvin-Helmholtz waves at the Earth's magnetopause: Multiscale
768 development and associated reconnection. J. Geophys. Res., 114, A12207.
769 doi:10.1029/2009JA014042
- 770 Haw, M. A., Seo, B., & Bellan, P. M. (2019). Laboratory measurement of large-amplitude
771 whistler pulses generated by fast magnetic reconnection. Geophysical Research Letters,
772 46, 7105-7112. <https://doi.org/10.1029/2019GL082621>
- 773 Hollweg, J. V. (1999). Kinetic Alfvén wave revisited. J. Geophys. Res., 104(A7), 14811-14819.
774 doi:10.1029/1998JA900132
- 775 Hu, Q., Zheng, J., Chen, Y., le Roux, J., & Zhao, L. (2018). Automated Detection of Small-scale
776 Magnetic Flux Ropes in the Solar Wind: First Results from the Wind Spacecraft
777 Measurements, Astrophysical Journal Supplement Series, 239, 12.
778 <https://doi.org/10.3847/1538-4365/aae57d>
- 779 Izutsu, T., Hasegawa, H., Nakamura, T. K. M., & Fujimoto, M. (2012) Plasma transport induced
780 by kinetic Alfvén wave turbulence. Phys. Plasmas, 19, 102305. doi:10.1063/1.4759167

- 781 Johnson, J. R., & Cheng, C. Z. (1997). Kinetic Alfvén waves and plasma transport at the
782 magnetopause. *Geophys. Res. Lett.*, 24, 1423-1426. <https://doi.org/10.1029/97GL01333>
- 783 Johnson, J. R., Cheng, C. Z., & Song, P. (2001). Signatures of mode conversion and kinetic
784 Alfvén waves at the magnetopause. *Geophys. Res. Lett.*, 28(2), 227-230.
785 <https://doi.org/10.1029/2000GL012048>
- 786 Johnson, J. R., & Cheng, C. Z. (2001). Stochastic ion heating at the magnetopause due to kinetic
787 Alfvén waves. *Geophys. Res. Lett.*, 28, 4421-4424.
788 <https://doi.org/10.1029/2001GL013509>
- 789 Karimabadi, H., Roytershteyn, V., Vu, H. X., et al. (2014). The link between shocks, turbulence,
790 and magnetic reconnection in collisionless plasmas. *Phys. Plasmas*, 21, 062308.
791 [doi:10.1063/1.4882875](https://doi.org/10.1063/1.4882875)
- 792 Lavraud, B., Thomsen, M. F., Lefebvre, B., Schwartz, S. J., Seki, K., Phan, T. D., Wang, Y. L.,
793 Fazakerley, A., Rème, H., & Balogh, A. (2006). Evidence for newly closed
794 magnetosheath field lines at the dayside magnetopause under northward IMF. *J.*
795 *Geophys. Res.*, 111, A05211. [doi:10.1029/2005JA011266](https://doi.org/10.1029/2005JA011266)
- 796 Li, W., André, M., Khotyaintsev, Yu. V., et al. (2016). Kinetic evidence of magnetic
797 reconnection due to Kelvin-Helmholtz waves. *Geophys. Res. Lett.*, 43, 5635-5643.
798 [doi:10.1002/2016GL069192](https://doi.org/10.1002/2016GL069192)
- 799 Lin, Y., Johnson, J. R., & Wang, X. Y. (2010). Hybrid simulation of mode conversion at the
800 magnetopause. *J. Geophys. Res.*, 115, A04208. [doi:10.1029/2009JA014524](https://doi.org/10.1029/2009JA014524)
- 801 Lin, Y., Johnson, J. R., & Wang, X. Y. (2012). Three-dimensional mode conversion associated
802 with kinetic Alfvén waves. *Phys. Rev. Lett.*, 109, 125003.
803 [doi:10.1103/PhysRevLett.109.125003](https://doi.org/10.1103/PhysRevLett.109.125003)
- 804 Lindqvist, P.-A., Olsson, G., Torbert, R. B., King, B., Granoff, M., et al. (2016). The Spin-plane
805 Double Probe electric field instrument for MMS. *Space Sci. Rev.*, 199, 137-165.
806 [doi:10.1007/s11214-014-0116-9](https://doi.org/10.1007/s11214-014-0116-9)
- 807 Matsumoto, Y., & Hoshino, M. (2004). Onset of turbulence induced by a Kelvin-Helmholtz
808 vortex. *Geophys. Res. Lett.*, 31, L02807. [doi:10.1029/2003GL018195](https://doi.org/10.1029/2003GL018195)
- 809 Matthaeus, W. H., Wan, M., Servidio, S., Greco, A., Osman, K. T., Oughton, S., & Dmitruk, P.
810 (2015). Intermittency, nonlinear dynamics and dissipation in the solar wind and
811 astrophysical plasmas. *Phil. Trans. R. Soc. A*, 373, 20140154.
812 <https://doi.org/10.1098/rsta.2014.0154>
- 813 Miesch, M. S., Elliott, J. R., Toomre, J., Clune, T. L., Glatzmaier, G. A., & Gilman, P. A. (2000).
814 Three-dimensional spherical simulations of solar convection. I. Differential rotation and
815 pattern evolution achieved with laminar and turbulent states. *Astrophys. J.*, 532, 593-615.
816 <https://doi.org/10.1086/308555>
- 817 Miura, A. (1997). Compressible magnetohydrodynamic Kelvin-Helmholtz instability with vortex
818 pairing in the two-dimensional transverse configuration. *Phys. Plasmas*, 4, 2871-2885.
819 <https://doi.org/10.1063/1.872419>

- 820 Nakamura, T. K. M., Fujimoto, M., & Otto, A. (2006). Magnetic reconnection induced by weak
 821 Kelvin-Helmholtz instability and the formation of the low-latitude boundary layer.
 822 *Geophys. Res. Lett.*, 33, L14106. doi:10.1029/2006GL026318
- 823 Nakamura, T. K. M., Hasegawa, H., Shinohara, I., & Fujimoto, M. (2011). Evolution of an
 824 MHD-scale Kelvin-Helmholtz vortex accompanied by magnetic reconnection: Two-
 825 dimensional particle simulations. *J. Geophys. Res.*, 116, A03227.
 826 doi:10.1029/2010JA016046
- 827 Nakamura, T. K. M., Daughton, W., Karimabadi, H., & Eriksson, S. (2013). Three-dimensional
 828 dynamics of vortex-induced reconnection and comparison with THEMIS observations. *J.*
 829 *Geophys. Res. Space Physics*, 118, 5742–5757. doi:10.1002/jgra.50547
- 830 Nakamura, T. K. M., Hasegawa, H., Daughton, W., Eriksson, S., Li, W. Y., & Nakamura, R.
 831 (2017). Turbulent mass transfer caused by vortex induced reconnection in collisionless
 832 magnetospheric plasmas. *Nature Communications*, 8, 1582. doi:10.1038/s41467-017-
 833 01579-0
- 834 Nakamura, T. K. M., Eriksson, S., Hasegawa, H., Zenitani, S., Li, W. Y., Genestreti, K. J.,
 835 Nakamura, R., and Daughton, W. (2017). Mass and energy transfer across the Earth’s
 836 magnetopause caused by vortex-induced reconnection. *Journal of Geophysical Research:*
 837 *Space Physics*, 122, 11505-11522, <https://doi.org/10.1002/2017JA024346>
- 838 Nakamura, T. K. M. (2019). The Earth’s low-latitude boundary layer, in *Magnetospheres in the*
 839 *Solar System* (eds. R Maggiolo, N. Andre, H. Hasegawa, & D. Welling), John Wiley &
 840 Sons, Inc, Hoboken, NJ.
- 841 Narita, Y., Gary, S. P., Saito, S., Glassmeier, K.-H., & Motschmann, U. (2011). Dispersion
 842 relation analysis of solar wind turbulence. *Geophys. Res. Lett.*, 38, L05101.
 843 doi:10.1029/2010GL046588
- 844 Narita, Y., Plaschke, F., Nakamura, R., et al. (2016). Wave telescope technique for MMS
 845 magnetometer. *Geophys. Res. Lett.*, 43, 4774-4780. doi:10.1002/2016GL069035
- 846 Narita, Y., Nakamura, R., Baumjohann, W., et al. (2016). On electron-scale whistler turbulence
 847 in the solar wind, *Astrophys. J. Lett.*, 827, L8, doi:10.3847/2041-8205/827/1/L8
- 848 Neubauer, F. M., & Glassmeier, K.-H. (1990). Use of an array of satellites as a wave telescope,
 849 *J. Geophys. Res.*, 95, 19115-19122. <https://doi.org/10.1029/JA095iA11p19115>
- 850 Nykyri, K., & Otto, A. (2001). Plasma transport at the magnetospheric boundary due to
 851 reconnection in Kelvin-Helmholtz vortices. *Geophys. Res. Lett.*, 28, 3565-3568.
 852 <https://doi.org/10.1029/2001GL013239>
- 853 Øieroset, M., Phan, T. D., Angelopoulos, V., Eastwood, J. P., McFadden, J., Larson, D., ...
 854 Raeder, J. (2008). THEMIS multi-spacecraft observations of magnetosheath plasma
 855 penetration deep into the dayside low-latitude magnetosphere for northward and strong
 856 by IMF. *Geophys. Res. Lett.*, 35, L17S11. <https://doi.org/10.1029/2008GL033661>
- 857 Paschmann, G., Baumjohann, W., Sckopke, N., Phan, T.-D., and Lühr, H. (1993). Structure of
 858 the dayside magnetopause for low magnetic shear. *J. Geophys. Res.*, 98(A8), 13409–
 859 13422. doi:10.1029/93JA00646

- 860 Phan, T. D., Eastwood, J. P., Shay, M. A., Drake, J. F., Sonnerup, B. U. Ö., et al. (2018).
 861 Electron magnetic reconnection without ion coupling in Earth's turbulent magnetosheath.
 862 *Nature*, 557, 202-206. doi:10.1038/s41586-018-0091-5
- 863 Pinçon, J. L., and Lefeuvre, F. (1991). Local characterization of homogeneous turbulence in a
 864 space plasma from simultaneous Measurements of field components at several points in
 865 space. *J. Geophys. Res.*, 96(A2), 1789-1802. doi:10.1029/90JA02183
- 866 Pollock, C., Moore, T., Jacques, A., et al. (2016). Fast Plasma Investigation for Magnetospheric
 867 Multiscale. *Space Sci. Rev.*, 199, 331-406. doi:10.1007/s11214-016-0245-4
- 868 Rezeau, L., & Belmont, G. (2001). Magnetic turbulence at the magnetopause, A key problem for
 869 understanding the solar wind/magnetosphere exchanges. *Space Sci. Rev.*, 95, 427-441.
 870 <https://doi.org/10.1023/A:1005273124854>
- 871 Russell, C. T., Anderson, B. J., Baumjohann, W., et al. (2016). The Magnetospheric Multiscale
 872 Magnetometers. *Space Sci. Rev.*, 199, 189-256. doi:10.1007/s11214-014-0057-3
- 873 Sahraoui, F., Goldstein, M. L., Robert, P., & Khotyaintsev, Y. V. (2009). Evidence of a cascade
 874 and dissipation of solar-wind turbulence at the electrons gyroscale. *Phys. Rev. Lett.*, 102,
 875 231102. doi:10.1103/PhysRevLett.102.231102
- 876 Sahraoui, F., Goldstein, M. L., Belmont, G., Canu, P., & Rezeau, L. (2010). Three dimensional
 877 anisotropic k spectra of turbulence at subproton scales in the solar wind. *Phys. Rev. Lett.*,
 878 105(13), 131101. doi:10.1103/PhysRevLett.105.131101
- 879 Smyth, W. D., & Moum, J. N. (2012). Ocean mixing by Kelvin-Helmholtz instability.
 880 *Oceanography*, 25(2), 140-149. <https://doi.org/10.5670/oceanog.2012.49>
- 881 Song, P., & Russell, C. T. (1992). Model of the formation of the low-latitude boundary layer for
 882 strongly northward interplanetary magnetic field. *J. Geophys. Res.*, 97(A2), 1411-1420.
 883 <https://doi.org/10.1029/91JA02377>
- 884 Stawarz, J. E., Eriksson, S., Wilder, F. D., et al. (2016). Observations of turbulence in a Kelvin-
 885 Helmholtz event on 8 September 2015 by the Magnetospheric Multiscale mission. *J.*
 886 *Geophys. Res. Space Physics*, 121. doi:10.1002/2016JA023458
- 887 Sturmer, A. P., Eriksson, S., Nakamura, T., Gershman, D. J., Plaschke, F., Ergun, R. E., et al.
 888 (2018). On multiple Hall-like electron currents and tripolar guide magnetic field
 889 perturbations during Kelvin-Helmholtz waves. *Journal of Geophysical Research: Space*
 890 *Physics*. 123, 1305-1324. <https://doi.org/10.1002/2017JA024155>
- 891 Vasavada, A. R., & Showman, A. P. (2005). Jovian atmospheric dynamics: an update after
 892 Galileo and Cassini. *Rep. Prog. Phys.*, 68, 1935. [https://doi.org/10.1088/0034-](https://doi.org/10.1088/0034-4885/68/8/R06)
 893 [4885/68/8/R06](https://doi.org/10.1088/0034-4885/68/8/R06)
- 894 Vernisse, Y., Lavraud, B., Eriksson, S., et al. (2016). Signatures of complex magnetic topologies
 895 from multiple reconnection sites induced by Kelvin-Helmholtz instability. *J. Geophys.*
 896 *Res. Space Physics*, 121, 9926-9939. doi:10.1002/2016JA023051
- 897 Wang, C.-P., Lyons, L. R., Nagai, T., Weygand, J. M., & Lui, A. T. Y. (2010). Evolution of
 898 plasma sheet particle content under different interplanetary magnetic field conditions. *J.*
 899 *Geophys. Res.*, 115, A06210. doi:10.1029/2009JA015028

- 900 Wang, C.-P., Fuselier, S. A., Hairston, M., Zhang, X.-j., Zou, S., Avakov, L. A., et al. (2019).
901 Event studies of O⁺ density variability within quiet-time plasma sheet. *Journal of*
902 *Geophysical Research: Space Physics*, 124, 4168-4187.
903 <https://doi.org/10.1029/2019JA026644>
- 904 Wing, S., Johnson, J. R., Newell, P. T., & Meng, C.-I. (2005). Dawn-dusk asymmetries, ion
905 spectra, and sources in the northward interplanetary magnetic field plasma sheet. *J.*
906 *Geophys. Res.*, 110, A08205. doi:10.1029/2005JA011086
- 907 Wilder, F. D., Ergun, R. E., Schwartz, S. J., et al. (2016). Observations of large-amplitude,
908 parallel, electrostatic waves associated with the Kelvin-Helmholtz instability by the
909 Magnetospheric Multiscale mission. *Geophys. Res. Lett.*, 43, 8859-8866.
910 doi:10.1002/2016GL070404
- 911 Wyngaard, J. C. (1992). Atmospheric turbulence. *Annu. Rev. Fluid Mech.*, 24, 205-234.
912 <https://doi.org/10.1146/annurev.fl.24.010192.001225>
- 913 Zimbardo, G., Greco, A., Sorriso-Valvo, L., et al. (2010). Magnetic turbulence in the geospace
914 environment. *Space Sci. Rev.*, 156, 89-134. doi:10.1007/s11214-010-9692-5
915

Figure 1.

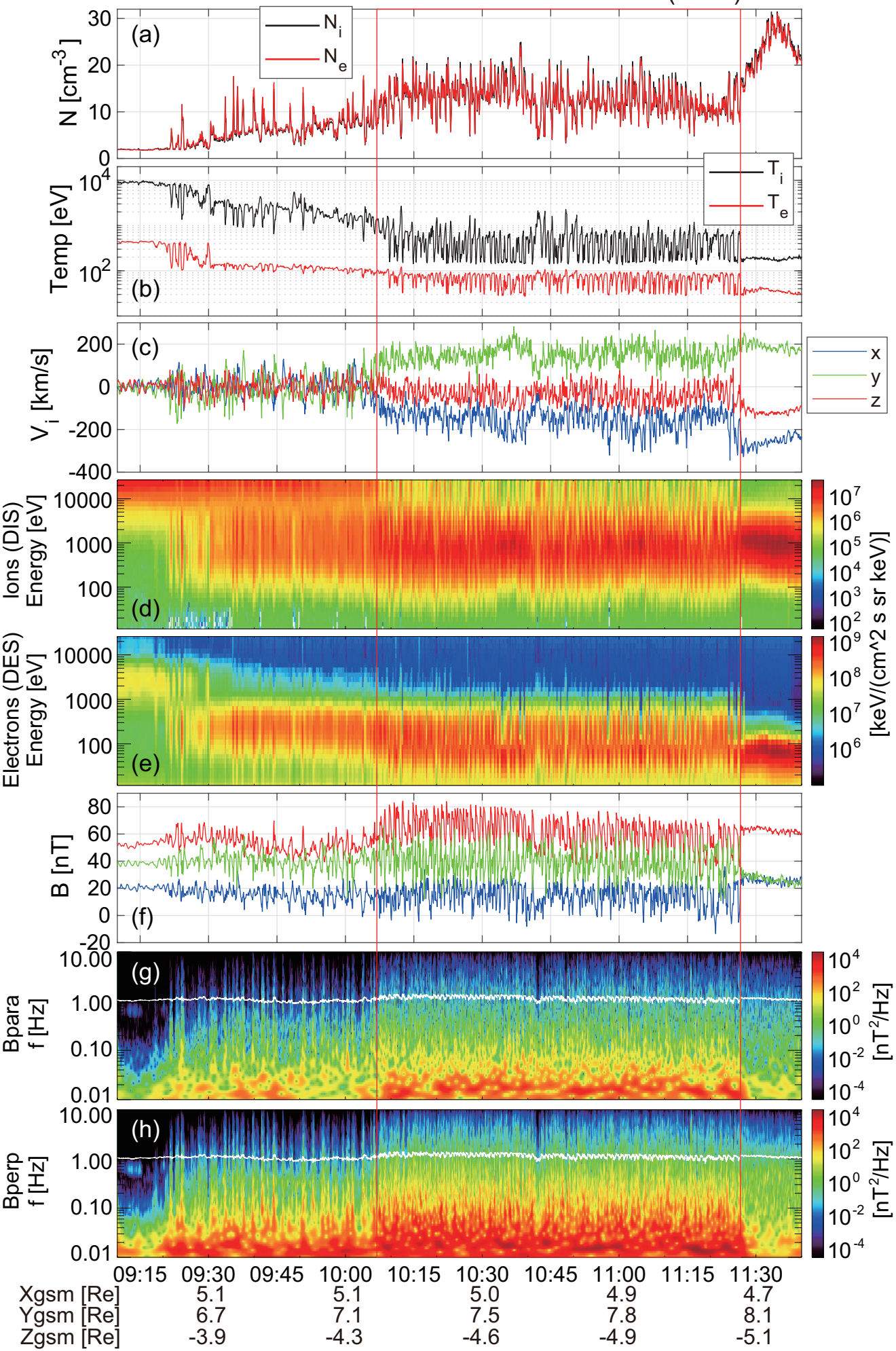
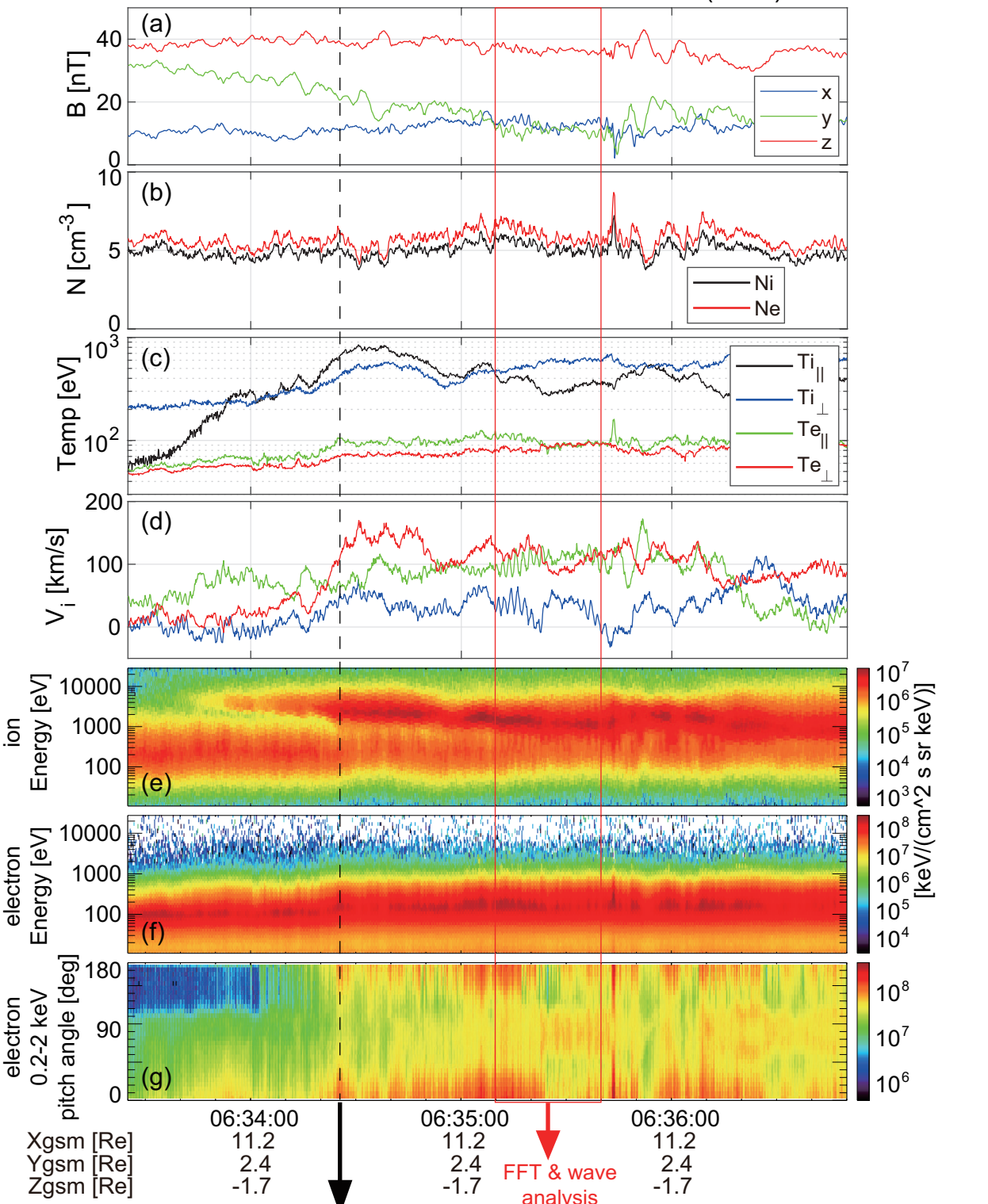
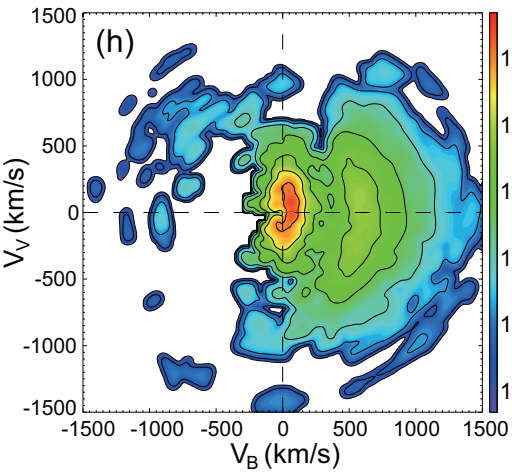


Figure 2.

MMS3 2015-11-08 0633:25 - 0636:50 UT (GSM)



Ion 2015-11-08/06:34:25.258 - 06:34:25.708 UT



Electron 2015-11-08/06:34:25.498 - 06:34:25.588

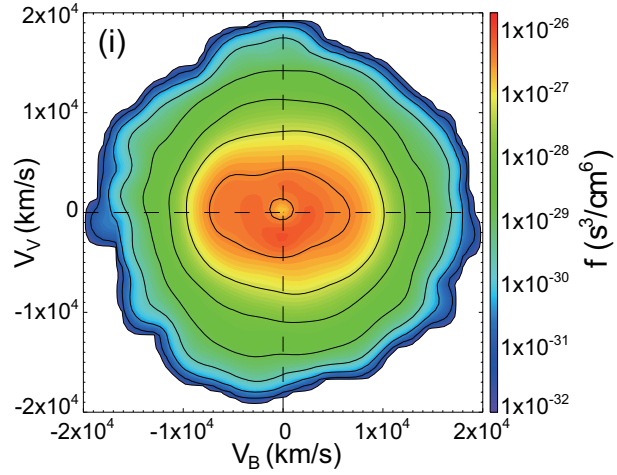
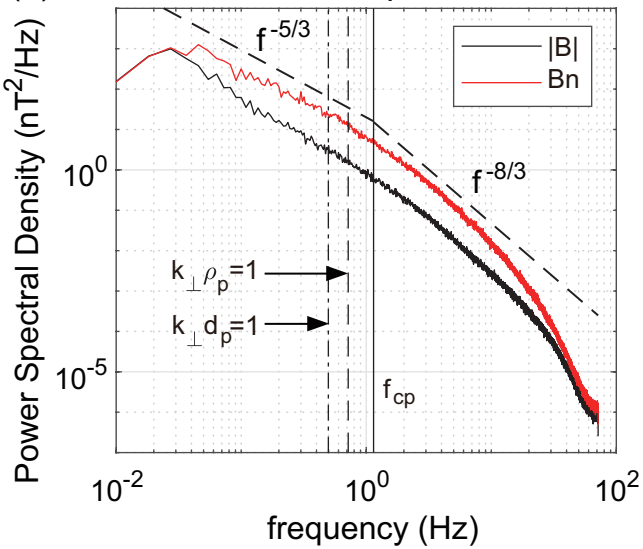


Figure 3.

(a) 2015-09-08 Mean spectra for KHI



(b) 2015-11-08 / 063510-063540 UT

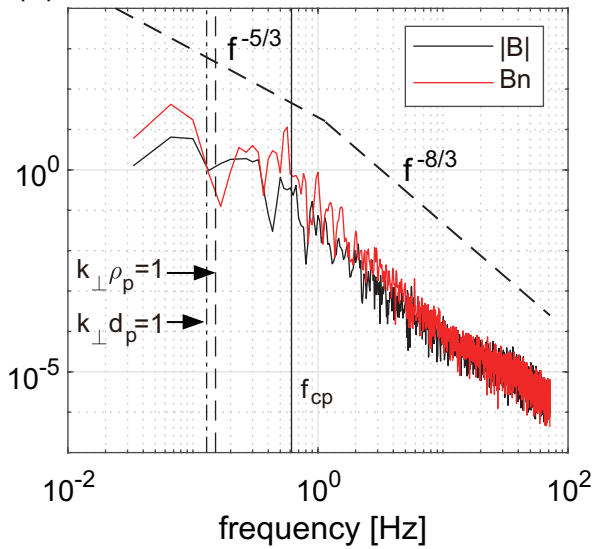


Figure 4.

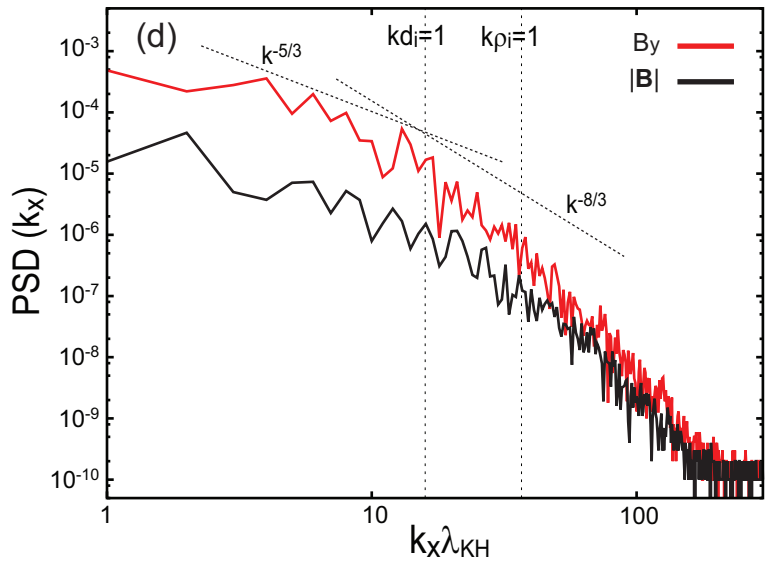
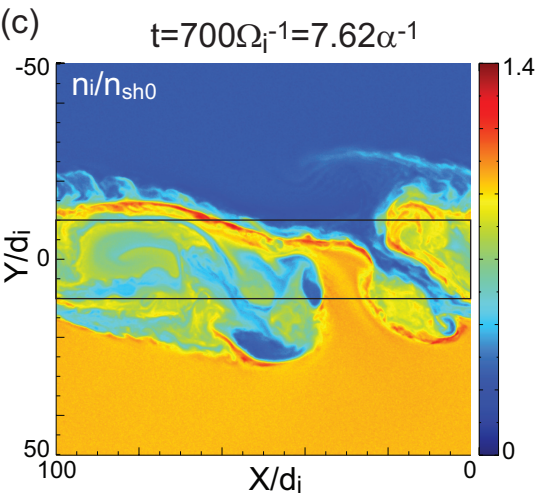
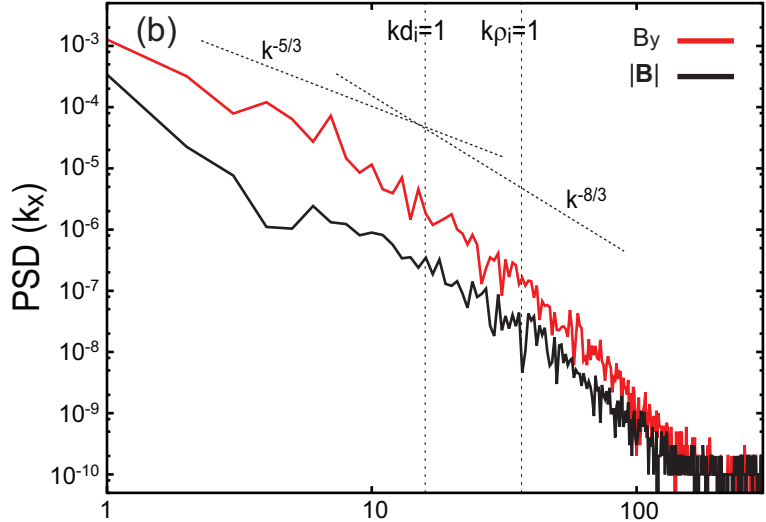
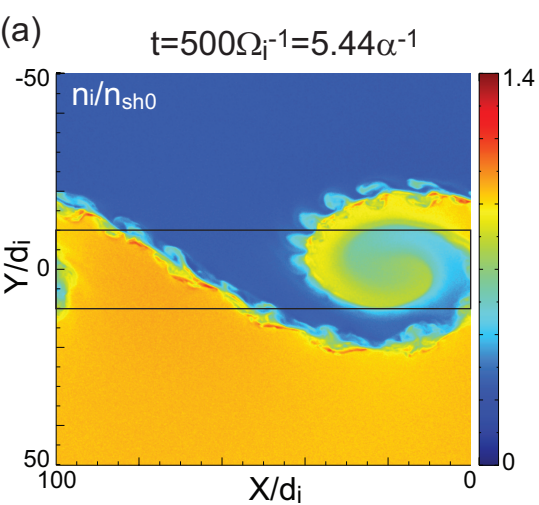
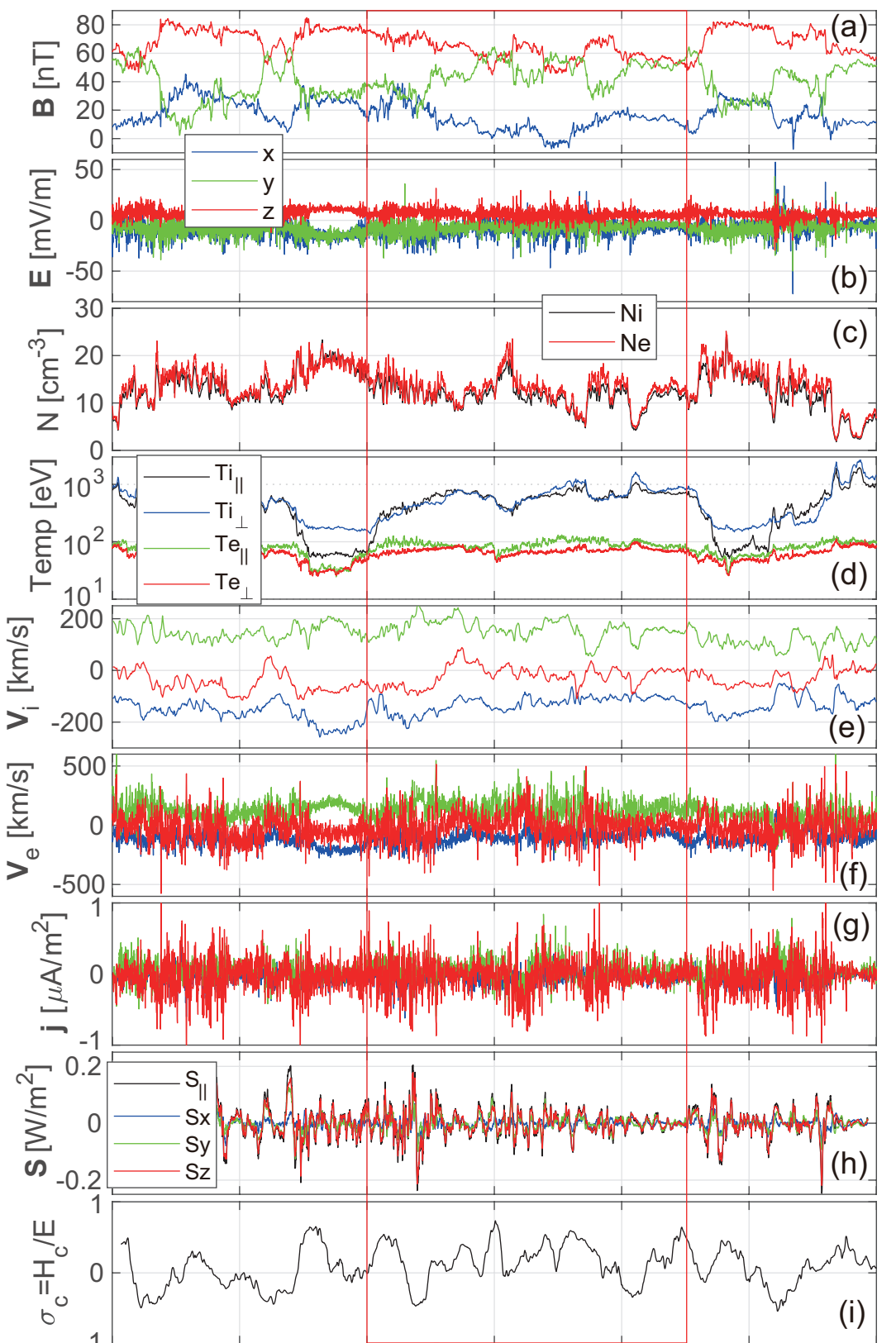


Figure 5.

MMS3 2015-09-08 1017:00 - 1017:00 UT



Xgsm [Re]	5.0	5.0	5.0
Ygsm [Re]	7.3	7.3	7.3
Zgsm [Re]	-4.5	-4.5	-4.5

Figure 6.

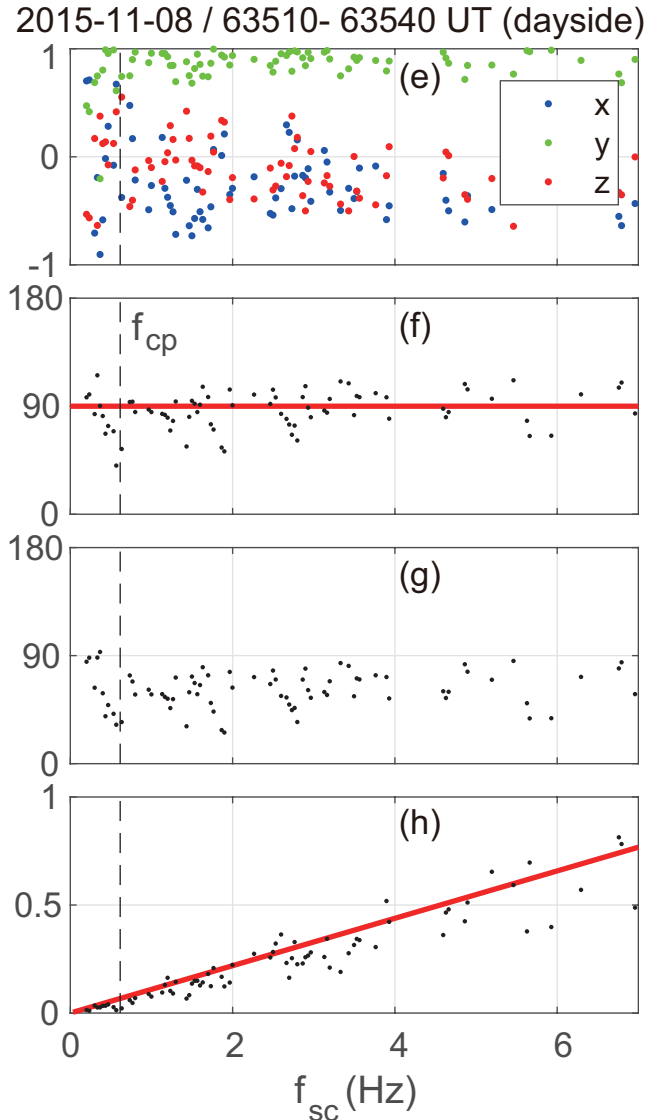
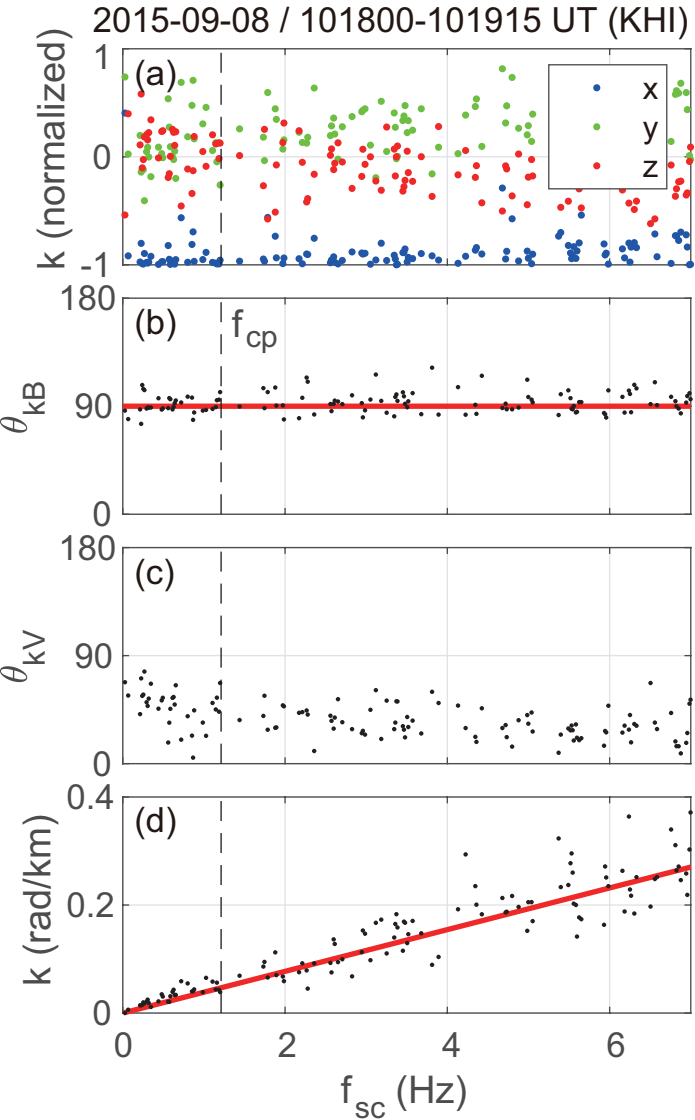
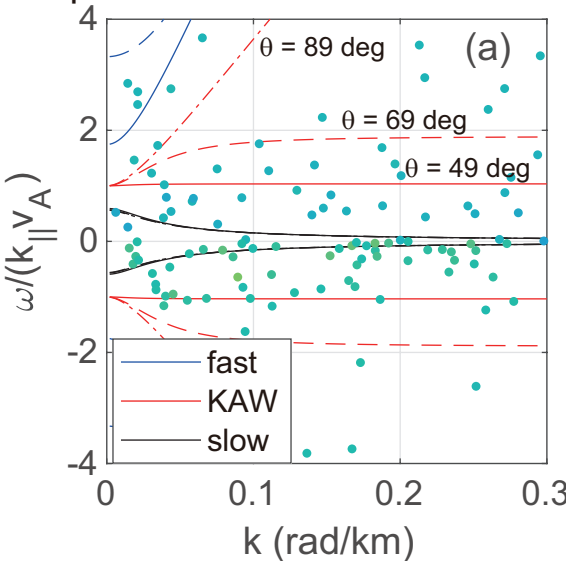


Figure 7.

Dispersion relation / 2015-09-08



Dispersion relation / 2015-11-08

